

A TVD neural network closure and application to turbulent combustion

Seung Won Suh*, Jonathan F. MacArt†, Luke N. Olson‡ and Jonathan B. Freund§

August 8, 2024

Abstract

Trained neural networks (NN) have attractive features for closing governing equations, but in the absence of additional constraints, they can stray from physical reality. A NN formulation is introduced to preclude spurious oscillations that violate solution boundedness or positivity. It is embedded in the discretized equations as a machine learning closure and strictly constrained, inspired by total variation diminishing (TVD) methods for hyperbolic conservation laws. The constraint is exactly enforced during gradient-descent training by rescaling the NN parameters, which maps them onto an explicit feasible set. Demonstrations show that the constrained NN closure model usefully recovers linear and nonlinear hyperbolic phenomena and anti-diffusion while enforcing the non-oscillatory property. Finally, the model is applied to subgrid-scale (SGS) modeling of a turbulent reacting flow, for which it suppresses spurious oscillations in scalar fields that otherwise violate the solution boundedness. It outperforms a simple penalization of oscillations in the loss function.

1 Introduction

Fully-resolved simulations of multiscale physical systems are often infeasible due to computational cost. To alleviate this, small scales are often unresolved or unrepresented, which reduces the predictive accuracy of the simulation. Many partial differential equation (PDE) models also employ reduced or uncertain models; for example, PDE models for reacting flow typically use simplified models for species diffusion and chemical kinetics [1]. With these factors degrading the fidelity of a simulation, it is desirable to represent unresolved and unknown or neglected physics using computationally efficient models.

Machine learning (ML) has become an attractive tool for this PDE closure challenge due to its model-form flexibility and the rapid advance of software and hardware support. We pursue a class of ML closures that embed a trainable neural network (NN) in a PDE model to represent missing or inaccurate terms [2, 3].

*Mechanical Science and Engineering, University of Illinois Urbana–Champaign, suh29@illinois.edu

†Aerospace and Mechanical Engineering, University of Notre Dame, jmacart@nd.edu

‡Computer Science, University of Illinois Urbana–Champaign, lukeo@illinois.edu

§Aerospace Engineering, University of Illinois Urbana–Champaign, jbfreund@illinois.edu

Specifically, we consider the following type of closure modeling problem:

$$\text{find } \vec{\theta} \tag{1.1a}$$

$$\text{that minimizes } \mathcal{J}[q, h, \vec{\theta}] \tag{1.1b}$$

$$\text{subject to } \partial_t q = R(q) + h(q; \vec{\theta}), \tag{1.1c}$$

where $q(\mathbf{x}, t)$ is a time t evolving solution over a space \mathbf{x} , $R(q)$ is the right-hand-side (RHS) term of the unclosed PDE, and $h(q; \vec{\theta})$ is a NN closure with N_θ trainable parameters $\vec{\theta} \in \mathbb{R}^{N_\theta}$. Altogether, (1.1c) is a NN-augmented PDE—serving as an optimization constraint—with $\mathcal{J}[q, h, \vec{\theta}] \in \mathbb{R}$ in (1.1b) the loss functional. This approach has been pursued for ML-based turbulence modeling with both *a priori* [4, 5, 6, 7] and *a posteriori* [2, 3, 8] training. Note that it is different from other ML strategies for PDEs, such as the Physics-Informed Neural Network (PINN) approach [9], the Deep Operator Network (DeepONet) [10], or the Deep Galerkin Method (DGM) [11], all of which train NNs to produce the solution directly without solving the PDE.

PDE-embedded models (NN-based or not) often require the preservation of certain solution properties for their numerical representation. For example, local conservation may be preserved exactly by casting the NN-augmented PDE into a discretely conservative form [8]. For the case of (1.1c), conservation may be ensured by replacing h with $-\nabla \cdot \mathbf{f}$, where ∇ is the divergence over \mathbf{x} , and \mathbf{f} is a vector-valued NN. Likewise, invariance properties may be leveraged by selecting invariant model inputs [7], and the symmetry of a NN model (e.g., to close the Reynolds stress tensor) may be enforced by modeling only independent components [2].

For any system with sharp features, such as shocks or flames, spurious (numerical) oscillations can violate physical boundedness and positivity constraints. Preventing this failure mode is challenging. Employing otherwise unneeded mesh resolution to suppress it can be prohibitively expensive, if it can work at all [12]. Numerical solutions of NN-embedded PDEs as in (1.1c) are also susceptible to constraint-violating spurious oscillations, and avoiding them is the goal of this paper.

Ideally, NN models could be trained to avoid spurious oscillations without explicitly enforcing the constraint. For example, if $\mathcal{J} \equiv D(q, q_e)$ measures the distance between q and a true solution q_e , then the model h would maintain smooth q (at least during training) if $\mathcal{J} = 0$ is exactly achieved. However, this is generally not the case. To illustrate this in a complex example, we preview simulation results from Section 3.5. Figure 1 visualizes results from a fine-mesh direct numerical simulation (DNS) of turbulent premixed flame and a corresponding coarse-mesh large-eddy simulation (LES) with a trained NN closure model. The challenge is that the reactant mass fraction Y in Fig. 1(d) from the LES violates $Y \in [0, 1]$, which can lead to additional violations for more complex physics. Simpler examples in Section 2.1 and Section 3 will illustrate how unconstrained NN closures suffer from spurious oscillations and how they can be avoided.

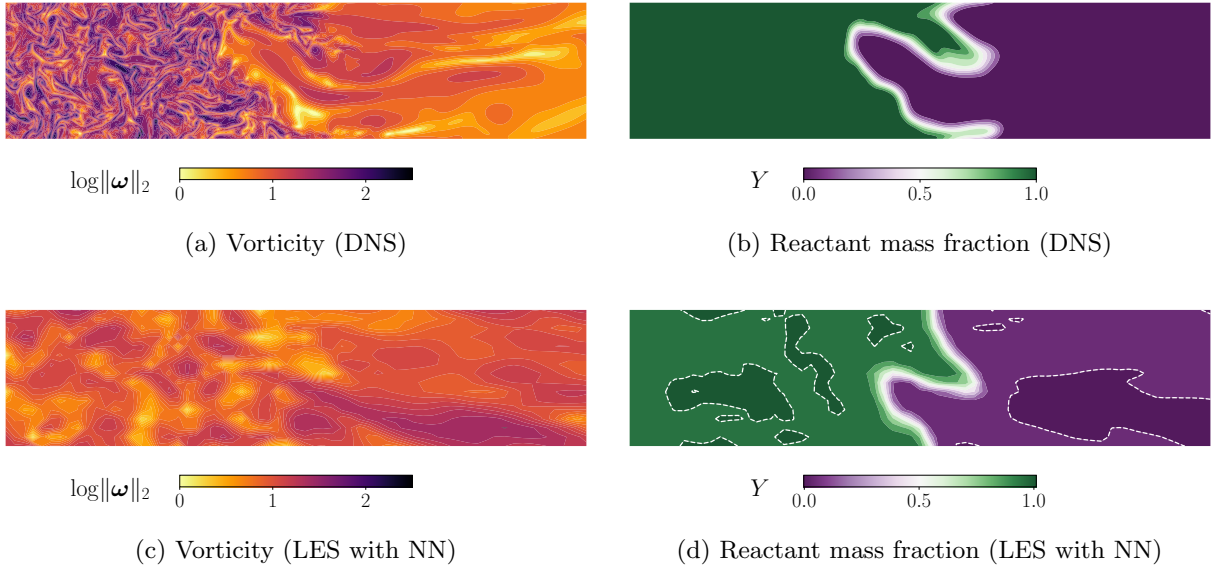


Figure 1: Simulations of three-dimensional turbulent premixed flames: (a, c) vorticity ω magnitude for (a) DNS, and (c) LES with trained NN closure; and (b, d) mass fraction Y of a reactant species for (b) DNS, and (d) LES with trained NN closure. Dashed contours in (d) indicate $Y = 0$ and $Y = 1$, and the constraint $Y \in [0, 1]$ is violated within the enclosed regions. Contours are plotted on a two-dimensional slice of the three-dimensional domain. The plot (d) is identical to Fig. 8(b).

To resolve this, the proposed formulation explicitly constrains the model in the optimization procedure:

$$\text{find } \vec{\theta} \tag{1.2a}$$

$$\text{that minimizes } \mathcal{J}[q, h, \vec{\theta}] \tag{1.2b}$$

$$\text{subject to } \partial_t q = R(q) + h(q; \vec{\theta}) \tag{1.2c}$$

$$\text{and } q \in \mathcal{Q}, \tag{1.2d}$$

where \mathcal{Q} is a space of nominally oscillation-free numerical solutions of the NN-augmented PDE (1.2c). Since the smoothness constraint is imposed on the solution q , not the NN parameters $\vec{\theta}$, the constraint cannot be enforced exactly, such as via projected gradient descent method [13, 14]. There is no means to find a feasible set of $\vec{\theta}$ that maps all the possible solutions q onto \mathcal{Q} in order to project $\vec{\theta}$. Of course, the constraint violation can be easily penalized via an enriched loss functional $\mathcal{J}' = \mathcal{J} + \mathcal{P}$, where $\mathcal{P} \geq 0$ becomes $\mathcal{P} = 0$ if q satisfies an oscillation-free condition. However, the resulting model is not guaranteed to exactly satisfy the constraint $\mathcal{P} = 0$, because gradient descent generally does not converge to the global optimum for a non-convex loss, and the conflict between \mathcal{J} and \mathcal{P} in multi-objective optimization precludes $\mathcal{P} = 0$ [15].

An alternative approach is to design h with constrained parameters $\vec{\theta}$ to guarantee that q is free of spurious oscillations so $\mathcal{P} = 0$ exactly. Such an h maps the q -constraint to a $\vec{\theta}$ -constraint as

$$\vec{\theta} \in \mathcal{C} \equiv \left\{ \vec{\theta} \mid q(\vec{\theta}) \in \mathcal{Q} \right\}, \tag{1.3}$$

so it can be strictly enforced on $\vec{\theta}$ via projected gradient descent:

$$\vec{\theta}^{k+1} = \pi_{\mathcal{C}} \left(\vec{\theta}^k - \bar{\alpha}^k \odot \frac{d\mathcal{J}^k}{d\vec{\theta}} \right), \tag{1.4}$$

where $\pi_{\mathcal{C}} : \mathbb{R}^{N_{\theta}} \rightarrow \mathcal{C}$ is a map onto the feasible set $\mathcal{C} \subseteq \mathbb{R}^{N_{\theta}}$, $\bar{\alpha}$ is the learning rate, and k denotes the gradient-descent iteration. In enforcing the constraint in *a posteriori* predictions, it is expected to outperform penalization. This is supported by Nair *et al.* [16], who trained NN closure models for transition-continuum flows with the Clausius–Duhem inequality enforced both strictly and loosely via penalization, showing that the strictly constrained model better extrapolates to out-of-sample flow conditions. Strict enforcement restricts h , though only in the spirit of the universal approximation theorem [17], which is predicated on a sufficiently effective NN model. We design and demonstrate a NN model h with parameters $\vec{\theta}$ that lie in \mathcal{C} , and that is sufficiently flexible to also usefully minimize \mathcal{J} .

This approach complements recent efforts to approximate PDEs with ML. Chen *et al.* [18] trained a NN flux to approximate one-dimensional hyperbolic PDEs by preserving the solution smoothness via the time integration scheme, but the NN flux closure itself was not limited to exactly preserve the property. Their previous work [19] made an important step in recognizing the challenge of spurious oscillations in the NN-predicted solutions. Kim and Kang [20] demonstrated their Fourier Neural Operator [21] for the same one-dimensional application but without focusing on this challenge.

The design of the new NN model h is discussed in Section 2, where the feasible set \mathcal{C} is also defined, and it is shown how to constrain $\vec{\theta}$ onto \mathcal{C} during optimization. In Section 3, the approach is demonstrated

on linear and nonlinear advection, a nonlinear hyperbolic system, a non-hyperbolic anti-diffusion problem, and the LES of turbulent reacting flow previewed in Fig. 1. In Section 4, the demonstrated capabilities are discussed along with potential extensions.

2 Model Design

2.1 Unconstrained NN challenge

We focus on PDEs for conservation laws, so we use conservation form $h = -\nabla \cdot \mathbf{f}$ in (1.1c) in the NN-augmented PDE

$$\partial_t q + \nabla \cdot \mathbf{f}(q; \vec{\theta}) = R(q) \quad (2.1)$$

where $\mathbf{f}(q; \vec{\theta})$ is the trainable NN flux closure.

We first illustrate the formation of spurious oscillations without the constraint. Consider a NN flux that is trained for a solution of a one-dimensional scalar conservation law. For simplicity, let $R = 0$, such that the NN model must represent the entirety of the physics. The optimization problem is then to

$$\text{find } \vec{\theta} \quad (2.2a)$$

$$\text{that minimizes } \mathcal{J} = D(q, q_e) \quad (2.2b)$$

$$\text{subject to } \partial_t q + \partial_x f(q; \vec{\theta}) = 0, \quad (2.2c)$$

where $q(x, t)$ is the solution predicted with the NN flux closure, $q_e(x, t)$ is a trusted (exact if available) solution of the PDE $\partial_t q + \partial_x f_e(q) = 0$ where f_e is the true flux, and $D(q, q_e)$ measures their mismatch. Then $\mathcal{J} \rightarrow 0$ implies $q \rightarrow q_e$ as well as $f \rightarrow f_e$.

For this demonstration, the model is trained for advection with unit speed $f_e(q) = q$ in a periodic domain $x \in [0, 1]$ for $t \in [0, t_f]$, where t_f is the final simulation time. Simple finite differencing of (2.2c) yields

$$q_i^n = q_i^{n-1} - \frac{\Delta t}{\Delta x} \left(f_{i+\frac{1}{2}}^{n-1} - f_{i-\frac{1}{2}}^{n-1} \right) \quad (2.3)$$

for $i \in \{0, 1, \dots, N_x - 1\}$ and $n \in \{1, \dots, N_t\}$, starting from the initial condition q_i^0 . Space is discretized as $x_i = i\Delta x$ with $\Delta x = 1/N_x$ where N_x is the number of independent grid points, and time is discretized as $t^n = n\Delta t$ with $\Delta t = t_f/N_t$ where N_t is the number of time steps. We use $N_x = 100$ so $\Delta x = 10^{-2}$, and $\Delta t = 2.5 \times 10^{-3}$. The discrete solution q_i^n approximates $q(x_i, t^n)$, and $f_{i+\frac{1}{2}}^n$ is the NN flux evaluated at the cell face $x_{i+\frac{1}{2}}$ using a two-point stencil:

$$f_{i+\frac{1}{2}}^n = f_{\mathcal{N}}(q_i^n, q_{i+1}^n; \vec{\theta}). \quad (2.4)$$

The flux $f_{\mathcal{N}}$ is a NN with a fully-connected feed-forward architecture [2]:

$$\begin{aligned}
z^1 &= \tanh(W^0 y + b^0) \\
z^2 &= \tanh(W^1 z^1 + b^1) \\
z^3 &= z^2 \odot g^1 \quad \text{with} \quad g^1 = \tanh(W^2 y + b^2) \\
z^4 &= \tanh(W^3 z^3 + b^3) \\
z^5 &= z^4 \odot g^2 \quad \text{with} \quad g^2 = \tanh(W^4 y + b^4) \\
\text{NN}(y; \vec{\theta}) &= W^5 z^5 + b^5
\end{aligned} \tag{2.5}$$

with parameters $\vec{\theta} \equiv \{W^i; b^i\}_{i=0}^5$. The two element-wise products \odot make the model capable of exactly representing third-order polynomials, while the tanh activation function will generally introduce additional nonlinearity [11]. We define a space of NN functions

$$\mathcal{N}(N_i \rightarrow N_h \rightarrow N_o) \equiv \{\text{NN}(y; \vec{\theta}) \mid W^0, W^2, W^4 \in \mathbb{R}^{N_h \times N_i}; W^1, W^3 \in \mathbb{R}^{N_h \times N_h}; W^5 \in \mathbb{R}^{N_o \times N_h}\}, \tag{2.6}$$

where N_i is the number of units in the input layer, N_h the units per hidden layer, and N_o the units in the output layer. In this demonstration, we use $N_h = 10$, so $f_{\mathcal{N}} \in \mathcal{N}(2 \rightarrow 10 \rightarrow 1)$. Although NN efficiency or accuracy might improve with adjustments, this architecture is sufficient for all our demonstrations.

The initial condition is

$$q(x, 0) = q_e(x, 0) = \begin{cases} 0 & 0 \leq x < 0.5 \\ 0.5 & x = 0.5 \\ 1 & 0.5 < x < 1, \end{cases} \tag{2.7}$$

which is evolved to $t_f = 0.2$ for $N_t = 80$ time steps, when the exact solution is $q_e(x, t_f) = q_e(x - t_f, 0)$. We define the loss as

$$\mathcal{J} = D(q, q_e) = \Delta x \sum_i \left[q(x_i, t_f; \vec{\theta}) - q_e(x_i, t_f) \right]^2. \tag{2.8}$$

Weights and biases of $f_{\mathcal{N}}$ are initialized with the Xavier initialization and trained by gradient descent using gradients computed with the full automatic differentiation (AD) provided by PyTorch [22]. Learning rates are adapted based on RMSprop [23] with the base learning rate of 10^{-3} , the smoothing constant of 0.99, and a small constant $\epsilon = 10^{-8}$ preventing division by zero.

Results are illustrated in Fig. 3, labeled “no constraint.” Figure 3(b) shows that 1000 training iterations decrease \mathcal{J} to about 10^{-3} of its initial value, suggesting that the model learns an operator consistent with the training data. However, the numerical solution in Fig. 3(a) oscillates rapidly near the sharp gradients, resembling typical artifacts from discretizing hyperbolic PDEs. There have been many efforts to develop numerical schemes that limit spurious oscillations for hyperbolic systems [24], yet they do not extend to NN training without additional development.

2.2 Constrained NN closure

2.2.1 Scalar advection in one dimension

The method developed here for simple scalar advection generalizes to the more involved cases considered subsequently. A starting point is to recognize how (2.3) also represents a finite-volume discretization of a scalar conservation law $\partial_t q + \partial_x f = 0$, where u_i^n and $f_{i+\frac{1}{2}}^n$ would correspond to the piecewise constant representation of the solution and the approximate numerical flux:

$$q_i^n = \frac{1}{\Delta x} \int_{x_{i-\frac{1}{2}}}^{x_{i+\frac{1}{2}}} q(x, t^n) dx \quad \text{and} \quad f_{i+\frac{1}{2}}^n = \frac{1}{\Delta t} \int_{t^n}^{t^{n+1}} f(q(x_{i+\frac{1}{2}}, t); \vec{\theta}) dt. \quad (2.9)$$

Non-oscillatory finite-volume schemes preserve the solution smoothness by properly limiting the numerical flux, which requires further development for our NN fluxes.

We start with Kurganov and Tadmor's (KT) central scheme [25]. This choice, which is made for simplicity, and other options are discussed in Section 4. Omitting time step indicator n from the notation, the flux f at $x_{i+\frac{1}{2}}$ is [25]

$$f_{i+\frac{1}{2}} = f^{\text{Rus}}(q_{i+\frac{1}{2}}^+, q_{i+\frac{1}{2}}^-; \vec{\theta}), \quad (2.10)$$

where f^{Rus} is the Rusanov flux for the NN $f_{\mathcal{N}}$

$$f^{\text{Rus}}(q_{i+\frac{1}{2}}^+, q_{i+\frac{1}{2}}^-; \vec{\theta}) = \frac{1}{2} \left[f_{\mathcal{N}}(q_{i+\frac{1}{2}}^+; \vec{\theta}) + f_{\mathcal{N}}(q_{i+\frac{1}{2}}^-; \vec{\theta}) - a_{i+\frac{1}{2}}(\vec{\theta})(q_{i+\frac{1}{2}}^+ - q_{i+\frac{1}{2}}^-) \right] \quad (2.11)$$

with the local maximum wave speed

$$a_{i+\frac{1}{2}}(\vec{\theta}) = \max \left[\left| f'_{\mathcal{N}}(q_{i+\frac{1}{2}}^+; \vec{\theta}) \right|, \left| f'_{\mathcal{N}}(q_{i+\frac{1}{2}}^-; \vec{\theta}) \right| \right]. \quad (2.12)$$

For this illustration, $f_{\mathcal{N}} \in \mathcal{N}(1 \rightarrow \cdot \rightarrow 1)$ is the needed single-input–single-output NN. Cell face values $q_{i+\frac{1}{2}}^\pm$ are the piecewise linearly reconstructed, slope-limited face states at $x_{i+\frac{1}{2}}$, from either the right (x_{i+1}) or the left (x_i) volumes:

$$q_{i+\frac{1}{2}}^+ = q_{i+1} - 0.5\phi(r_{i+1})(q_{i+2} - q_{i+1}) \quad \text{and} \quad q_{i+\frac{1}{2}}^- = q_i + 0.5\phi(r_i)(q_{i+1} - q_i), \quad (2.13)$$

where

$$r_i = \frac{q_i - q_{i-1}}{q_{i+1} - q_i} \quad (2.14)$$

is the ratio of neighboring slopes, and $\phi(r) = \max[0, \min(1, r)]$ is the minmod limiter [26]. The derivative of $f_{\mathcal{N}}$ as in (2.12) can be computed exactly by AD evaluation of

$$f'_{\mathcal{N}}(q_{i+\frac{1}{2}}^\pm; \vec{\theta}) = \frac{\partial}{\partial q_{i+\frac{1}{2}}^\pm} \sum_j f_{\mathcal{N}}(q_{j+\frac{1}{2}}^\pm; \vec{\theta}). \quad (2.15)$$

Figure 2 illustrates how the constrained overall model (2.10) can be regarded as constructed from the \mathcal{N} model, augmented with additional operations on its input and output: the input is pre-processed by (2.13) and the output is post-processed by (2.11). The NN $f_{\mathcal{N}}$ itself also needs to satisfy the Courant–Friedrichs–Lewy (CFL) condition while being trained, which will be discussed in Section 2.3, particularly (2.24).

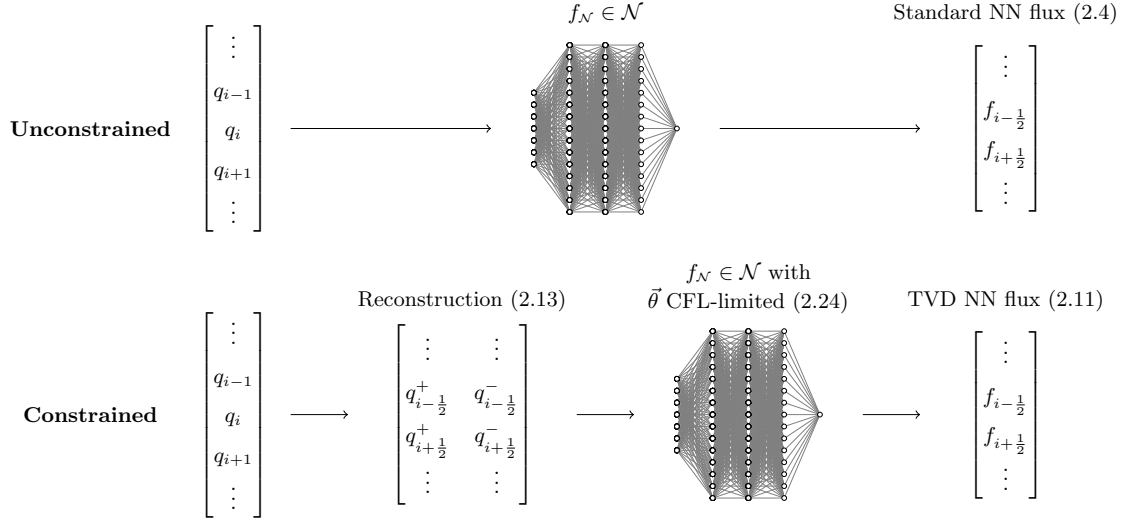


Figure 2: Schematic illustrating the difference between the unconstrained and the constrained NN closure.

What most directly provides the non-oscillatory property is the post-processing stage—the Rusanov flux (2.11)—which, from the usual finite-volume perspective, adds numerical dissipation. The pre-processing—slope-limited reconstruction (2.13)—reduces the numerical dissipation, preserving the resolution. It is important to note that for the NN model, the Rusanov flux alone is insufficient to unconditionally constrain the model since the model parameters $\vec{\theta}$ must also be adjusted to satisfy the CFL constraint. Only together do these stages complete the strict enforcement.

We designate the constrained version a “TVD NN closure,” where TVD indicates “total variation diminishing,” in the spirit of finite-volume TVD schemes [27]. In general, a numerical scheme or a numerical solution is called TVD if the total variation in space is non-increasing, with the total variation defined as

$$\text{TV}[q] = \sum_i |q_{i+1} - q_i|. \quad (2.16)$$

We use “TVD NN flux” to refer to the flux f in (2.10), constructed from f_N in (2.11). The divergence of f is embedded in the RHS of the PDE. As such, a TVD NN closure is a model composed of TVD NN fluxes. It will be demonstrated in Section 3 that the TVD NN closure does indeed preserve the TVD property.

2.2.2 Systems of equations in one dimension

Extension to systems of equations is straightforward. The corresponding PDE system with d state variables

$$\vec{q}_i^n = \begin{bmatrix} q_{1,i}^n \\ \vdots \\ q_{d,i}^n \end{bmatrix} = \begin{bmatrix} q_1(x_i, t^n) \\ \vdots \\ q_d(x_i, t^n) \end{bmatrix} \quad (2.17)$$

evolves as

$$\vec{q}_i^n = \vec{q}_i^{n-1} - \frac{\Delta t}{\Delta x} \left(\vec{f}_{i+\frac{1}{2}}^{n-1} - \vec{f}_{i-\frac{1}{2}}^{n-1} \right). \quad (2.18)$$

Following standard developments [25], the numerical flux \vec{f} is defined again via the Rusanov flux \vec{f}^{Rus} , again omitting the superscript n for convenience:

$$\vec{f}_{i+\frac{1}{2}} = \vec{f}^{\text{Rus}}(\vec{q}_{i+\frac{1}{2}}^+, \vec{q}_{i+\frac{1}{2}}^-; \vec{\theta}) = \frac{1}{2} \left[\vec{f}_{\mathcal{N}}(\vec{q}_{i+\frac{1}{2}}^+; \vec{\theta}) + \vec{f}_{\mathcal{N}}(\vec{q}_{i+\frac{1}{2}}^-; \vec{\theta}) - a_{i+\frac{1}{2}}(\vec{\theta})(\vec{q}_{i+\frac{1}{2}}^+ - \vec{q}_{i+\frac{1}{2}}^-) \right], \quad (2.19)$$

where

$$a_{i+\frac{1}{2}}(\vec{\theta}) = \max \left[\sigma \left(\frac{\partial \vec{f}_{\mathcal{N}}}{\partial \vec{q}} (\vec{q}_{i+\frac{1}{2}}^+) \right), \sigma \left(\frac{\partial \vec{f}_{\mathcal{N}}}{\partial \vec{q}} (\vec{q}_{i+\frac{1}{2}}^-) \right) \right]. \quad (2.20)$$

The $\vec{f}_{\mathcal{N}} \in (d \rightarrow \cdot \rightarrow d)$ is a NN model with d inputs and d outputs, and $\sigma(A)$ is the spectral radius of any matrix A . Computing the exact spectral radius of the Jacobian $\partial \vec{f}_{\mathcal{N}} / \partial \vec{q}$ requires both constructing the matrix and computing its eigenvalues. As a simpler alternative, which especially simplifies the AD-based training, an upper bound of the spectral radius can be computed directly as

$$\sigma \left(\frac{\partial \vec{f}_{\mathcal{N}}}{\partial \vec{q}} \right) \leq \left\| \frac{\partial \vec{f}_{\mathcal{N}}}{\partial \vec{q}} \right\|_1 = \max_{1 \leq j \leq d} \sum_{i=1}^d \left| \frac{\partial (f_{\mathcal{N}})_i}{\partial q_j} \right|, \quad (2.21)$$

with the 1-norm of the Jacobian now used for the nominal wave speed:

$$a_{i+\frac{1}{2}}(\vec{\theta}) = \max \left[\left\| \frac{\partial \vec{f}_{\mathcal{N}}}{\partial \vec{q}} (\vec{q}_{i+\frac{1}{2}}^+) \right\|_1, \left\| \frac{\partial \vec{f}_{\mathcal{N}}}{\partial \vec{q}} (\vec{q}_{i+\frac{1}{2}}^-) \right\|_1 \right]. \quad (2.22)$$

The consequence of this estimate is only that the scheme is more dissipative.

2.2.3 Multiple dimensions

Extension to multiple dimensions follows by applying the one-dimensional schemes in each spatial direction.

For example, in two dimensions with $\mathbf{x} = [x_1, x_2]^\top$, (2.18) becomes

$$\vec{q}_{i,j}^n = \vec{q}_{i,j}^{n-1} - \frac{\Delta t}{\Delta x_1} (\vec{f}_{i+\frac{1}{2},j}^{n-1} - \vec{f}_{i-\frac{1}{2},j}^{n-1}) - \frac{\Delta t}{\Delta x_2} (\vec{g}_{i,j+\frac{1}{2}}^{n-1} - \vec{g}_{i,j-\frac{1}{2}}^{n-1}), \quad (2.23)$$

where $\vec{q}_{i,j} = \vec{q}(x_{1,i}, x_{2,j}) = \vec{q}(i\Delta x_1, j\Delta x_2)$, and $\vec{f}_{i+\frac{1}{2},j}$ and $\vec{g}_{i,j+\frac{1}{2}}$ are TVD NN fluxes evaluated on the cell faces at $(i + \frac{1}{2}, j)$ and $(i, j + \frac{1}{2})$, respectively. The three-dimensional turbulent flame example in Section 3.5 uses a straightforward extension of this.

2.3 Constrained training via projected gradient descent

As already discussed in Section 2.2.1, a CFL condition is a key ingredient to avoid spurious oscillations:

$$\max_i a_{i+\frac{1}{2}}(\vec{\theta}) \Delta t / \Delta x \leq \text{CFL}_{\max}. \quad (2.24)$$

The maximum allowable value of the CFL number depends on the discretization and the time integration method. Central schemes—based on Nessyahu and Tadmor’s scheme [28], including the KT scheme—in one dimension with forward Euler time stepping have $\text{CFL}_{\max} = 1/2$.

A challenge is that $\max_i a_{i+\frac{1}{2}}(\vec{\theta})$ varies during training as the NN parameters adjust each iteration as $\vec{\theta}^{k+1} = \vec{\theta}^k - \vec{\alpha}^k \odot (\text{d}\mathcal{J}^k/\text{d}\vec{\theta})$. For an arbitrary Δt , it is probable that the maximum wave speed will exceed the limit in (2.24) during training. To prevent this and to achieve TVD, we define the feasible set of $\vec{\theta}$ as

$$\mathcal{C} = \left\{ \vec{\theta} \mid \max_i a_{i+\frac{1}{2}}(\vec{\theta}) \leq \text{CFL}_{\max} \Delta x / \Delta t \right\}, \quad (2.25)$$

and the updated weights are mapped onto \mathcal{C} every iteration,

$$\vec{\theta}^{k+1} = \pi_{\mathcal{C}} \left(\vec{\theta}^k - \vec{\alpha}^k \odot \frac{\text{d}\mathcal{J}^k}{\text{d}\vec{\theta}} \right), \quad (2.26)$$

ensuring that the model satisfies the constraint exactly. Since the spectral radius (or the 1-norm) of the Jacobian $\partial \vec{f}_{\mathcal{N}} / \partial \vec{q}$ scales as the output layer of the NN, rescaling its weights keeps the maximum wave speed bounded. The map $\pi_{\mathcal{C}}$ is thus taken to be a simple rescaling of the weights of the output layer:

$$\pi_{\mathcal{C}}(W^l) = \begin{cases} \frac{\text{CFL}_{\max} \Delta x / \Delta t}{\max_{i,n} a_{i+\frac{1}{2}}^n(\vec{\theta})} W^l & l = 5 \quad \text{and} \quad \max_{i,n} a_{i+\frac{1}{2}}^n(\vec{\theta}) > \text{CFL}_{\max} \Delta x / \Delta t \\ W^l & \text{otherwise.} \end{cases} \quad (2.27)$$

This map onto \mathcal{C} is sufficient but not unique, and it might warrant additional investigation. In (2.27), $\max_{i,n} a_{i+\frac{1}{2}}^n(\vec{\theta})$ is the maximum wave speed over all grid points i and all time steps n in evaluating \mathcal{J} .

3 Demonstrations

3.1 One-dimensional advection

We first demonstrate the TVD NN model on the Section 2.1 case, with the NN trained to learn the RHS of the one-dimensional advection equation based on the optimization scenario (2.2). The flux f is represented by the TVD NN (2.10) with $f_{\mathcal{N}} \in \mathcal{N}(1 \rightarrow 10 \rightarrow 1)$. Parameters are again Xavier initialized and optimized with RMSprop using the same hyperparameters as in Section 2.1.

Figure 3(a) compares $q(x, t_f)$ numerical solutions for both cases with the exact solution. Both successfully identify the underlying advection physics, which is confirmed by the learning curves in Fig. 3(b). Of course, the strictly enforced constraint restricts the loss reducing capacity of the model, so the loss for the TVD NN is larger, but only the unconstrained NN introduces obvious spurious oscillations. Figure 3(c) shows that the TVD NN is, in fact, TVD with the TV value deviating from its initial value only by $\mathcal{O}(10^{-14})$, whereas the unconstrained model has qualitatively incorrect oscillations.

3.2 Burgers equation

Application to the inviscid Burgers equation $\partial_t q + \partial_x(q^2/2) = 0$ demonstrates extension to nonlinear dynamics. Again, the NN is required to learn the entire RHS, and $f_{\mathcal{N}} \in \mathcal{N}(1 \rightarrow 10 \rightarrow 1)$ provides the TVD NN, with $f_{\mathcal{N}} \in \mathcal{N}(2 \rightarrow 10 \rightarrow 1)$ for the corresponding unconstrained case. The discretization matches that

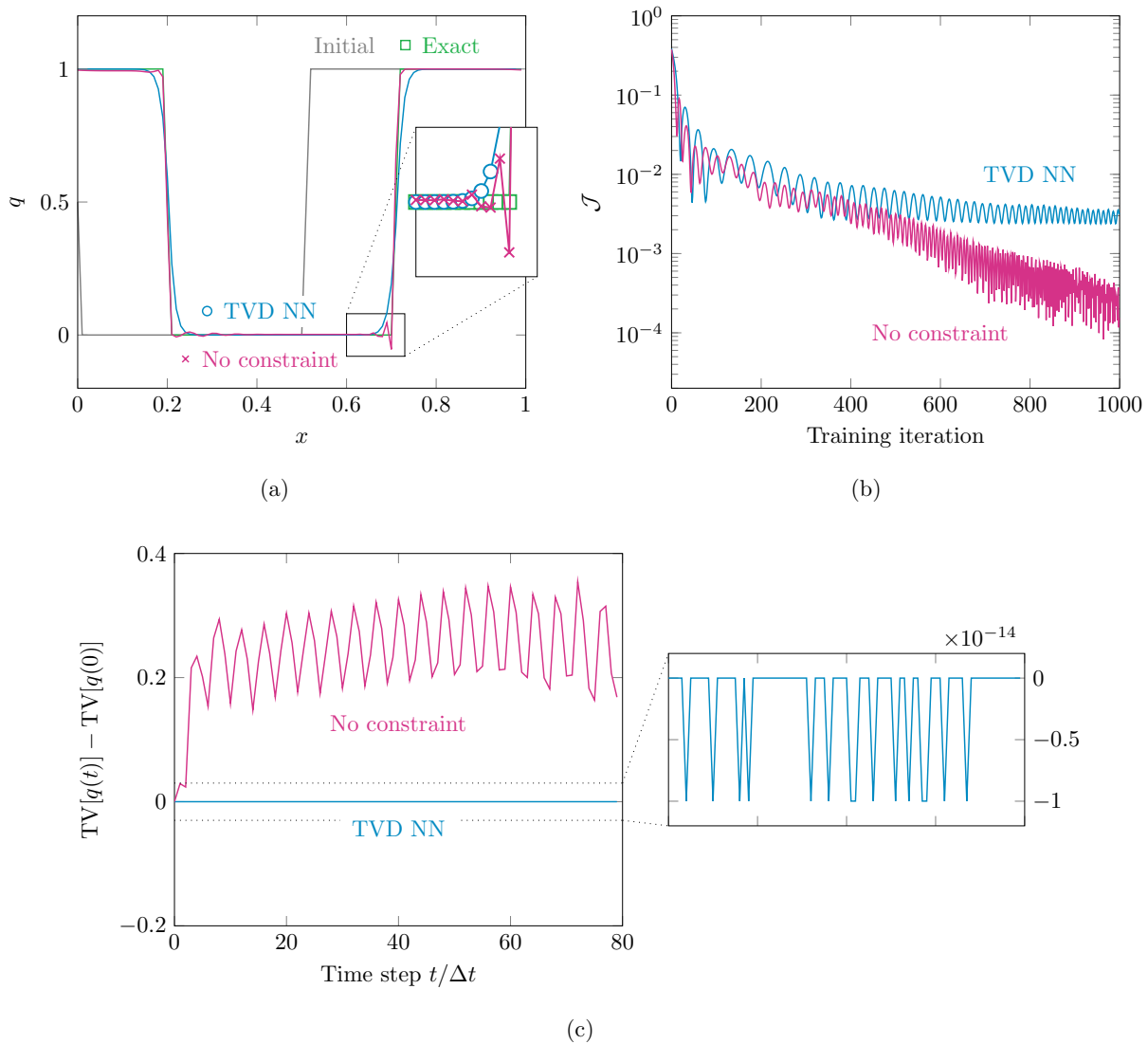


Figure 3: Demonstration for the one-dimensional advection $\partial_t q + \partial_x q = 0$. (a) The unconstrained and the TVD NN predictions at $t = t_f$; (b) learning curves of both models; and (c) TV (2.16) deviations from initial values.

used for the linear advection with 100 grid points on periodic $x \in [0, 1]$ and 80 time steps until $t_f = 0.25$. The initial profiles for q and the exact solution q_e are discontinuous:

$$q(x, 0) = q_e(x, 0) = \begin{cases} 1 & 0.375 \leq x < 0.625 \\ 0 & \text{otherwise,} \end{cases} \quad (3.1)$$

with the exact solution

$$q_e(x, t_f) = \begin{cases} 0 & 0 \leq x < 0.375 \\ 4(x - 0.375) & 0.375 \leq x < 0.625 \\ 1 & 0.625 \leq x < 0.75 \\ 0 & 0.75 \leq x < 1. \end{cases} \quad (3.2)$$

The loss is again defined as (2.8). RMSprop with the same hyperparameters as before is used for optimization.

Figure 4 shows that the TVD NN prediction is close to the exact solution without the spurious oscillations of the unconstrained NN. Again, the unconstrained model reaches a lower \mathcal{J} but at the expense of introducing oscillations. In Fig. 4(c), the TV value for the TVD NN decreases by a non-negligible amount after 60 time steps as the trained model overly dissipates the solution, though it only suggests that our model is TVD.

3.3 One-dimensional Euler equations

In this case, a NN flux \vec{f} from (2.18) is trained to learn the full RHS of the one-dimensional Euler equations based on its prediction of the conserved variables

$$\vec{q} = \begin{bmatrix} \rho \\ \rho u \\ E \end{bmatrix}, \quad (3.3)$$

where ρ is the density, u the velocity, and E the total energy. The exact flux is

$$\vec{f}_e(\vec{q}) = \begin{bmatrix} \rho u \\ \rho u^2 + p \\ u(E + p) \end{bmatrix}, \quad (3.4)$$

with $\gamma = 1.4$ providing pressure $p = (\gamma - 1)(E - \rho u^2/2)$. The model is trained to match the exact solution \vec{q}_e with the loss defined as

$$\mathcal{J} = \Delta x \sum_i \left\| \vec{q}(x_i, t_f; \vec{\theta}) - \vec{q}_e(x_i, t_f) \right\|_2^2. \quad (3.5)$$

We expect that $\vec{f} \rightarrow \vec{f}_e$ once \mathcal{J} is minimized.

The TVD property for a system of PDEs is more complex than the case of a single scalar equation. For example,

$$\text{TV}[\vec{q}] = \sum_i \|\vec{q}_{i+1} - \vec{q}_i\|_1 \quad (3.6)$$

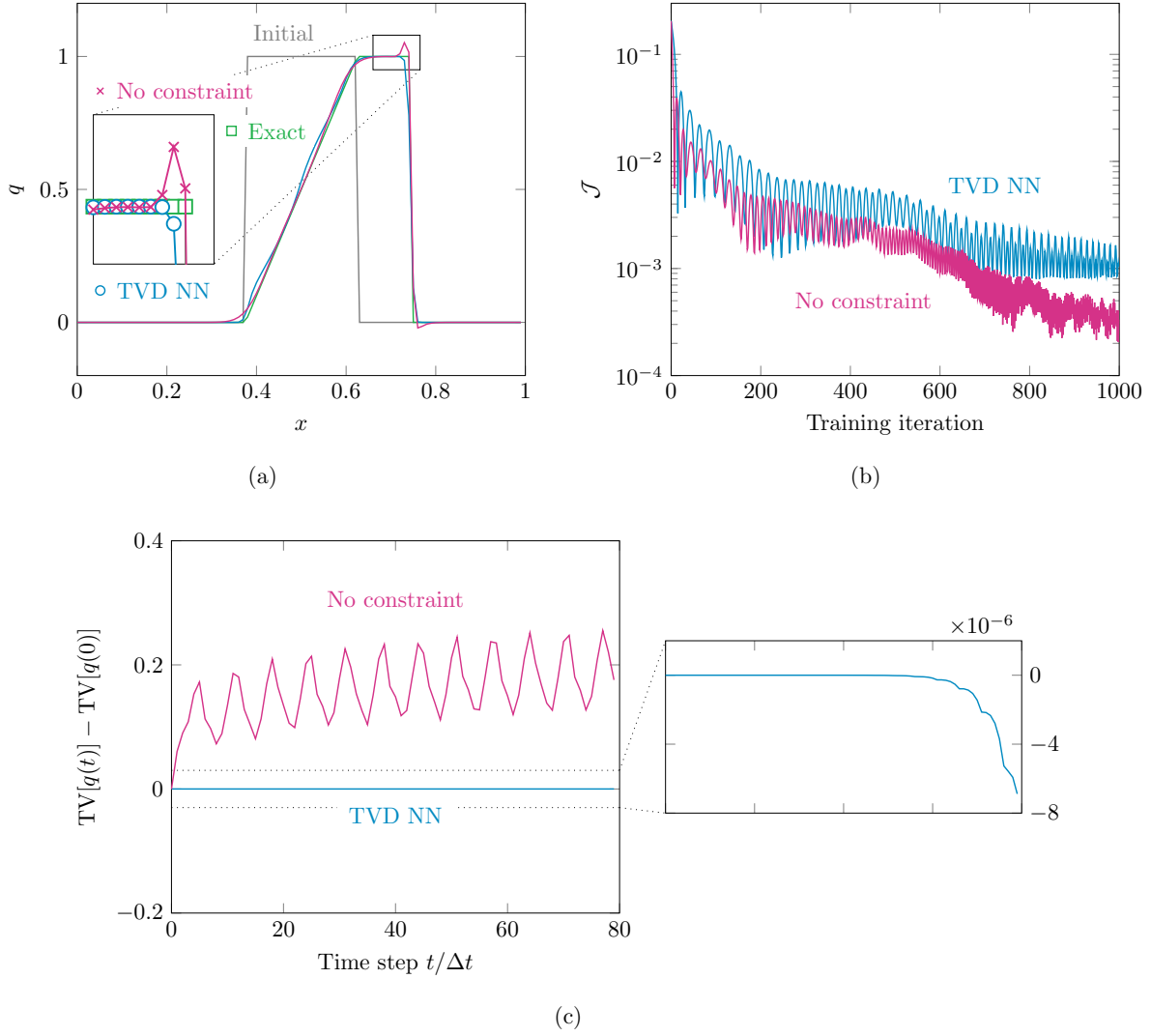


Figure 4: Demonstration for the one-dimensional Burgers equation $\partial_t q + \partial_x(q^2/2) = 0$. (a) Model predictions at $t = t_f$; (b) learning curves of both models; and (c) TV (2.16) deviations from initial values.

is insufficient to check the TVD property of a scheme because the exact solution \vec{q}_e itself may have increasing total variation. For a system, one way is to measure the total variation of the amplitude of characteristic waves. This can be done analytically for certain PDEs, including the Euler equations; however, in general, the decomposition can be cumbersome [29, Section 15]. As a result, we do not monitor the exact TVD property of the scheme for systems, though the benefits will be obvious.

The spatial domain $x \in [0, 1]$ is discretized in the same manner as the scalar case with 501 mesh points, including boundary points, yielding $\Delta x = 2 \times 10^{-3}$. Time is discretized as $\Delta t = 10^{-4}$ over $t \in [0.1, 0.15]$. The model prediction \vec{q} is initialized at $t = 0.1$ with $\vec{q}_e(x, t = 0.1)$ and we compare the solutions at $t_f = 0.15$. The exact solution \vec{q}_e follows the Sod configuration [30] with the initial condition

$$\vec{q}_e(x, 0) = \begin{cases} \vec{q}_L & x < 0.5 \\ \vec{q}_R & x \geq 0.5 \end{cases}, \quad \vec{q}_L = \begin{bmatrix} 1.0 \\ 1.0 \\ 0.0 \end{bmatrix}, \quad \vec{q}_R = \begin{bmatrix} 0.125 \\ 0.1 \\ 0.0 \end{bmatrix}. \quad (3.7)$$

Early $t \in [0, 0.1]$ is not used for training to focus on the richer behavior that follows the step initial condition. In particular, testing for $t \in [0, 0.1]$ yields excellent suppression of oscillations but poor learning of physics underlying the moving discontinuities.

The solution features do not reach the boundaries of the domain, so homogeneous Neumann boundary conditions are sufficient at $x = 0$ and 1 . The constrained NN model is $\vec{f}_{\mathcal{N}} \in \mathcal{N}(3 \rightarrow 50 \rightarrow 3)$ while the unconstrained model is also based on the formulation (2.18) but with $\vec{f}_{i+\frac{1}{2}} = \vec{f}_{\mathcal{N}}(\vec{q}_i, \vec{q}_{i+1}; \vec{\theta}) \in \mathcal{N}(6 \rightarrow 50 \rightarrow 3)$. Again, RMSprop is used for the training with the same hyperparameter values as before. All the weights except for the output layer W^5 are Xavier initialized; W^5 is initialized as zero to prevent an unnecessary overshoot of \mathcal{J} in early gradient descent iterations.

Figure 5 shows that both NN models successfully reproduce the gross features, as might be expected for a similar finite-volume scheme, reducing the loss significantly, but the TVD NN also suppresses oscillations. Loss oscillating at $\mathcal{J} \lesssim 10^{-3}$ for both cases is expected as the model nears a local minimum and RMSprop starts searching more broadly around it.

3.4 One-dimensional advection with anti-diffusion

Thus far, only hyperbolic systems have been considered with clear TVD properties. A final example, before the application to turbulent combustion, is not hyperbolic. This requires a modification of the formulation. Since $f_{\mathcal{N}}$ in (2.11) and $\vec{f}_{\mathcal{N}}$ in (2.19) are local, depending only on pointwise grid values, both are only capable of learning hyperbolic behaviors. It cannot represent a diffusion-like behavior, which is more fundamentally nonlocal and can, therefore, be expected to require multi-point input like a finite difference gradient. We generalize the model design to address this.

The most convenient example would be advection-diffusion; however, significant diffusion so readily suppresses oscillation that a more illustrative scenario involves an anti-diffusive flux that triggers instabilities.

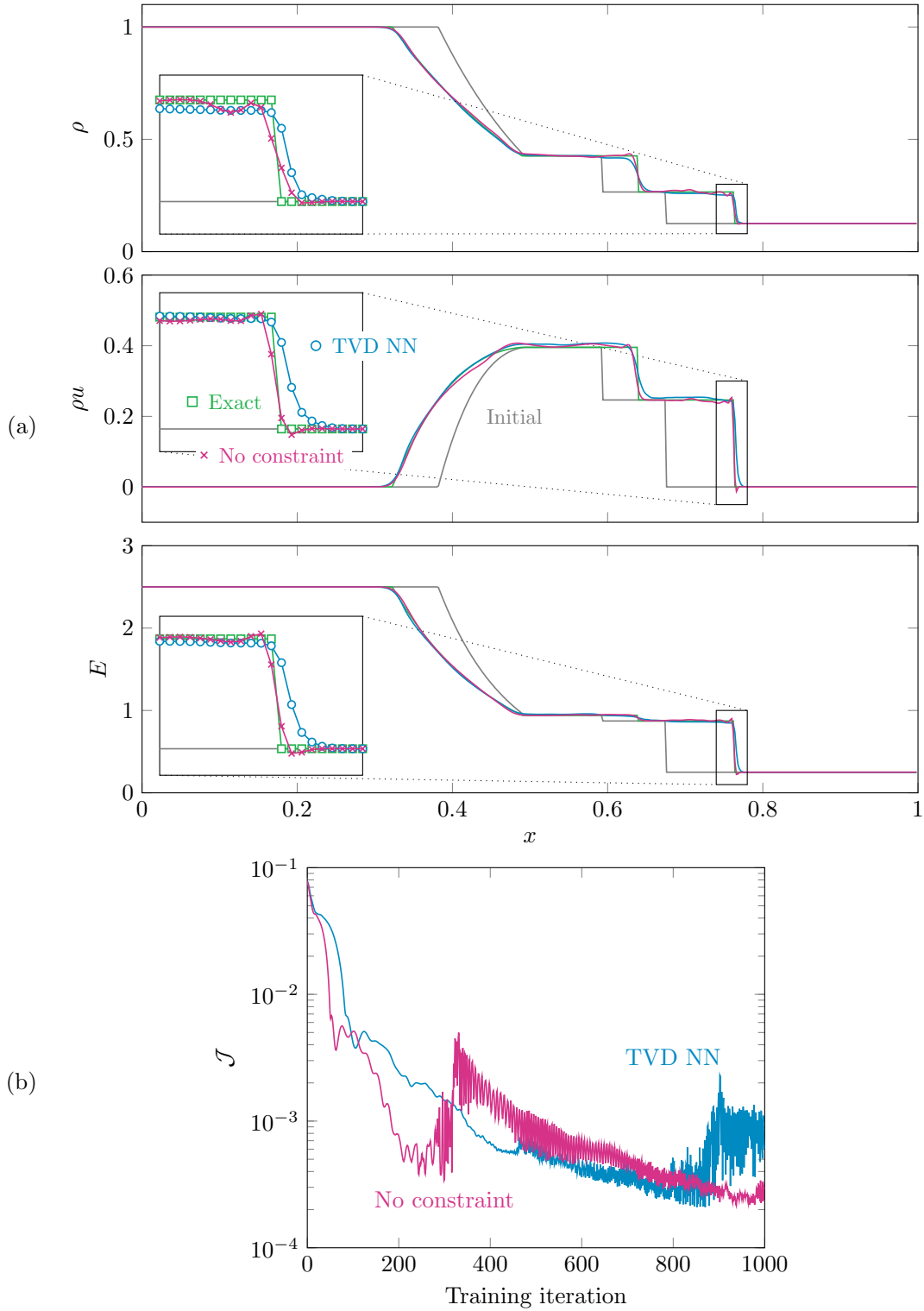


Figure 5: Demonstration for the one-dimensional Euler equations. (a) Numerical solutions of $\vec{q}(x, t_f)$ predicted by both models, initial conditions, and the analytical solutions; (b) learning curves of both models.

Anti-diffusion is also relevant to turbulent flames. For example, consider the filtered transport equation of a flame progress variable c for LES:

$$\begin{aligned}\frac{\partial \bar{\rho} \tilde{c}}{\partial t} &= -\nabla \cdot (\bar{\rho} \tilde{\mathbf{u}} c) - \nabla \cdot (\bar{\rho} \tilde{\boldsymbol{\varphi}}_c) + \bar{\omega}_c \\ &= -\nabla \cdot (\bar{\rho} \tilde{\mathbf{u}} \tilde{c}) - \nabla \cdot (\bar{\rho} \tilde{\boldsymbol{\varphi}}_c) + \bar{\omega}_c - \nabla \cdot (\bar{\rho} \boldsymbol{\varphi}_c^r),\end{aligned}\quad (3.8)$$

where \mathbf{u} is the flow velocity, $\dot{\omega}_c$ the production rate of c by chemical reaction, and $\boldsymbol{\varphi}_c$ the diffusive flux. Given a variable q , $\bar{q} = \mathcal{F}q$ and $\tilde{q} = \mathcal{F}\rho q / \mathcal{F}\rho$ denote its filtered and Favre-filtered values, respectively, by a filter \mathcal{F} . For this illustration, only the sub-filter-scale convection $\boldsymbol{\varphi}_c^r = \tilde{\mathbf{u}}c - \tilde{\mathbf{u}}\tilde{c}$ is considered in (3.8); filtered terms involving $\tilde{\boldsymbol{\varphi}}_c$ and $\bar{\omega}_c$ are left unclosed. A common gradient-diffusion model is $\boldsymbol{\varphi}_c^r = -\mathcal{D}_T \nabla \tilde{c}$ with the eddy diffusivity \mathcal{D}_T . However, this assumes that $\boldsymbol{\varphi}_c^r$ is aligned with $\nabla \tilde{c}$, but near a flame, $\boldsymbol{\varphi}_c^r$ can be counter to the gradient [31, 32], which warrants an anti-diffusive flux. A NN closure model for $\boldsymbol{\varphi}_c^r$ will be most effective if it is capable of learning anti-diffusion. Of course, unconstrained anti-diffusion introduces spurious oscillations, leading eventually to unbounded \tilde{c} . In combustion, violations of $\tilde{c} \in [0, 1]$ as seen in Fig. 1, where $Y = 1 - \tilde{c}$, are qualitatively incorrect, and similar out-of-bound behaviors can have challenging consequences for more complex physiochemical models.

Based on (2.10), the numerical flux for a one-dimensional scalar is generalized as

$$f_{i+\frac{1}{2}} = \frac{1}{2} \left[f_{\mathcal{N}}(q_{i+\frac{1}{2}}^+; \bar{\boldsymbol{\theta}}_f) + f_{\mathcal{N}}(q_{i+\frac{1}{2}}^-; \bar{\boldsymbol{\theta}}_f) - a_{i+\frac{1}{2}}(\bar{\boldsymbol{\theta}}_f)(q_{i+\frac{1}{2}}^+ - q_{i+\frac{1}{2}}^-) \right] - \hat{\nu}_{i+\frac{1}{2}} \frac{q_{i+1} - q_i}{\Delta x}, \quad (3.9)$$

where $\hat{\nu}_{i+\frac{1}{2}}$ is the NN-predicted local diffusivity. To limit the anti-diffusive contribution of $\hat{\nu}$, it is decomposed into two parts:

$$\hat{\nu}_{i+\frac{1}{2}} = \left| \nu_{\mathcal{N}}^+(q_i, q_{i+1}; \bar{\boldsymbol{\theta}}_{\nu^+}) \right| + \psi(r_i, r_{i+1}) \nu_{\mathcal{N}}^-(q_i, q_{i+1}; \bar{\boldsymbol{\theta}}_{\nu^-}), \quad (3.10)$$

where $|\nu_{\mathcal{N}}^+|$ and $\nu_{\mathcal{N}}^-$ represent the diffusive and potentially anti-diffusive components, respectively. Both $\nu_{\mathcal{N}}^+$ and $\nu_{\mathcal{N}}^-$ are $\in \mathcal{N}(2 \rightarrow \cdot \rightarrow 1)$. While $\nu_{\mathcal{N}}^+$ is cast positive as $|\nu_{\mathcal{N}}^+|$ so its effect is strictly diffusive, $\nu_{\mathcal{N}}^-$ is not, but ψ limits its anti-diffusive effect based on the shape of the solution:

$$\psi(r_i, r_{i+1}) = \begin{cases} \min[\min(r_i, 1/r_i), \min(r_{i+1}, 1/r_{i+1})] & \min(r_i, r_{i+1}) > 0 \\ 0 & \text{otherwise,} \end{cases} \quad (3.11)$$

where r_i is the same ratio of neighboring slopes defined in (2.14). For this demonstration, a small number $\epsilon_r = 10^{-12}$ is added to the denominator to prevent division by zero as

$$r_i = \frac{q_i - q_{i-1}}{q_{i+1} - q_i + \epsilon_r}. \quad (3.12)$$

Figure 6 sketches the mechanism of the flux limiter: anti-diffusion is permitted only when the sequence $(q_{i-1}, q_i, q_{i+1}, q_{i+2})$ is monotone—when both r_i and r_{i+1} are positive. If either q_i or q_{i+1} is a local extremum, $\psi(r_i, r_{i+1})$ is zero, suppressing anti-diffusion. Anti-diffusivity $\psi \nu_{\mathcal{N}}^-$ is maximized when $r_i = r_{i+1} = 1$, which corresponds to a locally linear profile.

The formulation is demonstrated for a solution with flame-like evolution from a smooth profile to a sharp discontinuity while being advected at a constant speed. A time-reversed heat equation solution is used to

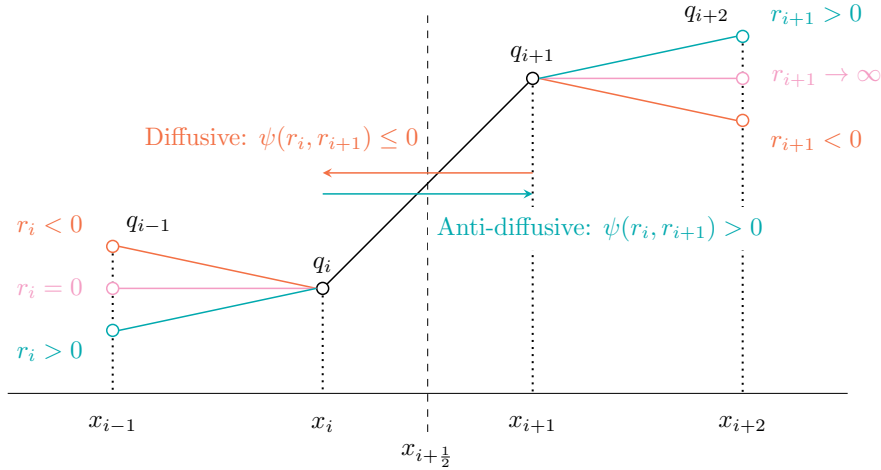


Figure 6: Action of the limiter for the anti-diffusive flux. Arrows indicate the direction of the $x_{i+\frac{1}{2}}$ flux.

construct the target solution for training. We define w the solution of $\partial_t w = \nu \partial_{xx} w$ with $\nu = 0.01$ with the initial condition

$$w(x, 0) = \begin{cases} 0 & 0 \leq x < 0.5 \\ 1 & 0.5 \leq x < 1 \end{cases} \quad (3.13)$$

on a periodic domain $x \in [0, 1]$. The target solution is $q_e(x, t) = w(x - t, t_f - t)$, which is the solution of the advection-anti-diffusion equation $\partial_t q + \partial_x q = -\nu \partial_{xx} q$ that evolves from smooth $w(x, t_f)$ at $t = 0$ to sharp $w(x - t_f, 0)$ at $t = t_f$. The NNs $f_{\mathcal{N}}$, $\nu_{\mathcal{N}}^+$, and $\nu_{\mathcal{N}}^-$ are trained simultaneously to minimize

$$\mathcal{J} = \Delta x \sum_i \left[q(x_i, t_f; \vec{\theta}) - q_e(x_i, t_f) \right]^2, \quad (3.14)$$

where $q(x, 0) = q_e(x, 0)$ and $\vec{\theta} = [\vec{\theta}_f; \vec{\theta}_{\nu^+}; \vec{\theta}_{\nu^-}]$. Here, the Section 2.1 discretization for both space and time is used with $t_f = 0.2$.

The NN models are $f_{\mathcal{N}} \in \mathcal{N}(1 \rightarrow 10 \rightarrow 1)$ and $\nu_{\mathcal{N}}^{\pm} \in \mathcal{N}(2 \rightarrow 10 \rightarrow 1)$, along with an unconstrained NN $f_{\mathcal{N}} \in \mathcal{N}(2 \rightarrow 10 \rightarrow 1)$ for comparison. A TVD NN closure model based on (2.11) without the $\hat{\nu}$ modification is also included for comparison. All models are trained using RMSprop with the same hyperparameters, and model parameters are Xavier initialized. The raw output of $\nu_{\mathcal{N}}^{\pm}$ is multiplied by the physical viscosity ν to provide a good initial guess to the training predictions, which helps prevent overshoots in early training iterations.

Numerical solutions predicted by all models are plotted in Fig. 7(a), and the learning curves and TV histories are plotted in Fig. 7(b) and Fig. 7(c). We observe that the constrained model with $\hat{\nu}$ successfully predicts the displaced and sharpened profile without the obvious oscillations of the unconstrained model. The TV value for the generalized model (3.9) increases but only slightly, which is due to the error introduced

in (3.12). Thus, we regard it bounded $q \in [0, 1]$ within tolerance as desirable for a flame progress variable. Oscillations in the unconstrained model (2.4) prediction are qualitatively different from typical spurious oscillations in hyperbolic problems. They even appear away from sharp gradients due to the anti-diffusion instability: in Fig. 7(c), the instability becomes obvious after around 15 time steps. The hyperbolic-only model (2.11) fails to learn effective anti-diffusion, showing that the nonlocal generalization of (3.9) is beneficial.

3.5 Premixed flame in three-dimensional turbulence

Finally, the TVD NN is applied to SGS modeling for the flame in a turbulent premixture of Fig. 1. The simulation is adapted from Towery *et al.* [33]. The nondimensional reacting compressible Navier–Stokes equations

$$\partial_t \vec{q} + \nabla \cdot \vec{\mathbf{f}}(\vec{q}) = \vec{\mathbf{s}}(\vec{q}) \quad (3.15)$$

for

$$\vec{q} = \begin{bmatrix} \rho \\ \rho \mathbf{u} \\ E \\ \rho Y \end{bmatrix}, \quad (3.16)$$

govern the flow, in a three-dimensional space $\mathbf{x} = [x_1, x_2, x_3]^\top$ and flow velocity $\mathbf{u} = [u_1, u_2, u_3]^\top$. The chemical reaction is taken to be single-species, single-step, and irreversible for the reactant mass fraction Y : a single reactant is perfectly converted to a product past the flame, so $Y = 1$ for reactant, and $Y = 0$ for the product. E is the sum of the internal and kinetic energy, not including the chemical energy. The transport flux and the non-conservative source term are

$$\vec{\mathbf{f}}(\vec{q}) = \begin{bmatrix} \rho \mathbf{u} \\ \rho \mathbf{u} \mathbf{u} + p \mathbf{I} \\ \mathbf{u}(E + p) \\ \rho \mathbf{u} Y \end{bmatrix} - \begin{bmatrix} 0 \\ \boldsymbol{\tau} \\ \boldsymbol{\tau} \cdot \mathbf{u} - \varphi_T \\ -\varphi_Y \end{bmatrix} \quad \text{and} \quad \vec{\mathbf{s}}(\vec{q}) = \begin{bmatrix} 0 \\ \mathbf{0} \\ Q \dot{\omega} \\ -\dot{\omega} \end{bmatrix}. \quad (3.17)$$

The viscous stress and diffusive fluxes are

$$\boldsymbol{\tau} = \frac{\mu}{\text{Re}} \left[\nabla \mathbf{u} + (\nabla \mathbf{u})^\top - \frac{2}{3} (\nabla \cdot \mathbf{u}) \mathbf{I} \right], \quad \varphi_T = -\frac{\mu}{\text{Re Pr}} \nabla T, \quad \text{and} \quad \varphi_Y = -\frac{\mu}{\text{Re Sc}} \nabla Y, \quad (3.18)$$

where Re is the Reynolds number, Pr the Prandtl number, and Sc the Schmidt number. The viscosity depends on the temperature T as $\mu = (T/T_0)^{0.7}$ with T_0 the unburnt gas temperature, and the ideal gas equation of state is $p = (\gamma - 1)\rho T/\gamma$, where the pressure is $p = (\gamma - 1)(E - \rho \mathbf{u} \cdot \mathbf{u}/2)$. The chemical reaction rate is $\dot{\omega} = A \rho^2 Y \exp[(\beta/\alpha)(1 - T_f/T)]$, in which A is the Arrhenius constant, α the heat release ratio, β the Zel'dovich number, $T_f = T_0/(1 - \alpha)$ the adiabatic flame temperature, and $Q = \alpha T_f$ the heat release parameter. See A.1 for more details, including the nondimensionalization and the parameter values.

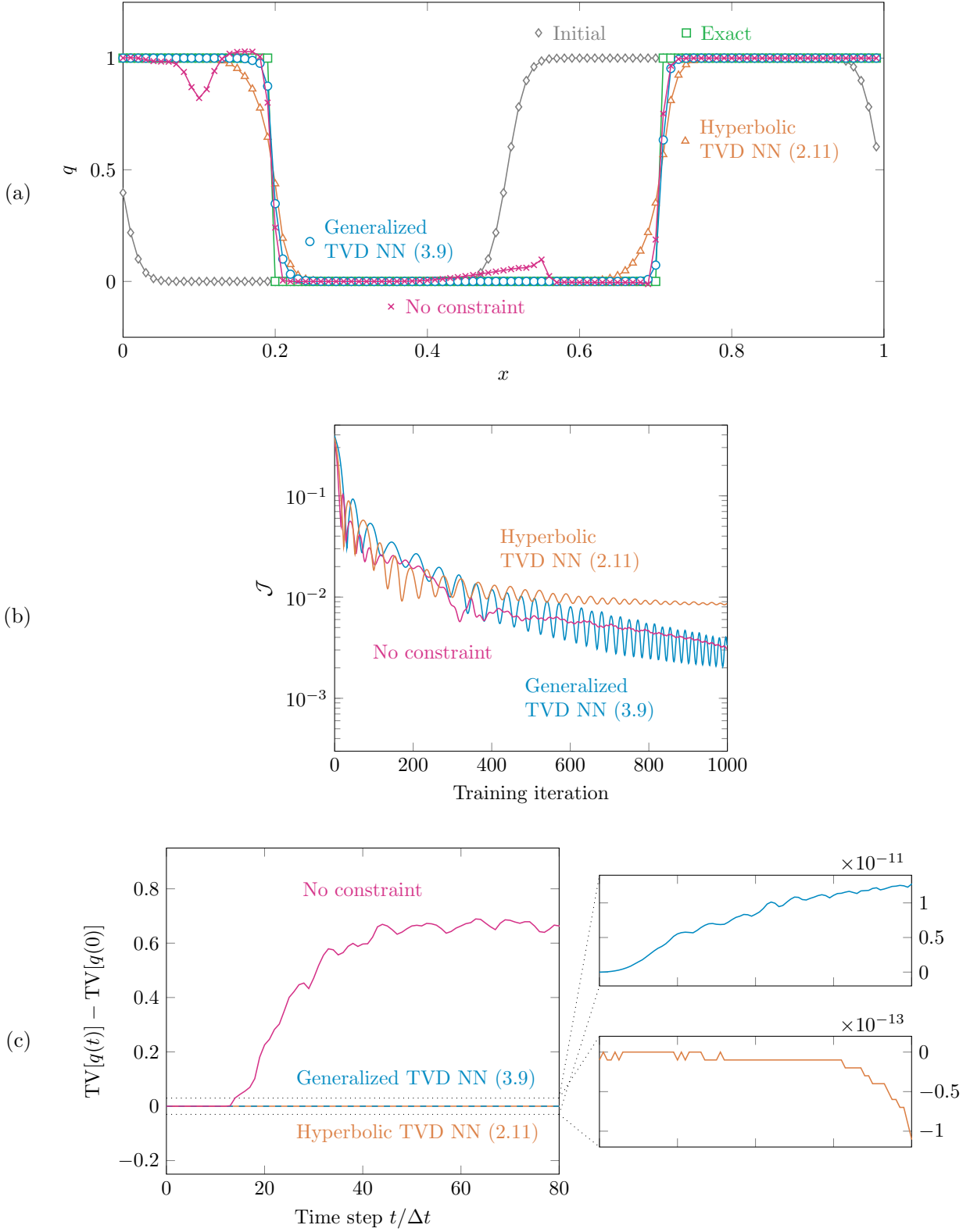


Figure 7: One-dimensional advection with anti-diffusion: (a) numerical solutions at $t = t_f$, the exact solution, and the initial condition; (b) learning curves; and (c) TV (2.16) deviations from initial values.

The governing equations are filtered and solved for the filtered state variables

$$\mathcal{F}_{\bar{\Delta}}\vec{q}(\mathbf{x}, t) = \int F_{\bar{\Delta}}(\mathbf{x} - \mathbf{x}')\vec{q}(\mathbf{x}', t) d\mathbf{x}', \quad (3.19)$$

where $F_{\bar{\Delta}}$ is a spatial filter kernel with its filter width $\bar{\Delta}$ defining the LES, and $\mathcal{F}_{\bar{\Delta}}$ is the corresponding filter operator. The governing equations for $\mathcal{F}_{\bar{\Delta}}\vec{q}$ are

$$\partial_t(\mathcal{F}_{\bar{\Delta}}\vec{q}) = -\nabla \cdot (\mathcal{F}_{\bar{\Delta}}\vec{\mathbf{f}}(\vec{q})) + \mathcal{F}_{\bar{\Delta}}\vec{s}'(\vec{q}) = -\nabla \cdot [\vec{\mathbf{f}}(\mathcal{F}_{\bar{\Delta}}\vec{q}) + \vec{\mathbf{f}}_e^r] + [\vec{s}(\mathcal{F}_{\bar{\Delta}}\vec{q}) + \vec{s}_e^r], \quad (3.20)$$

where the exact unclosed residuals are

$$\vec{\mathbf{f}}_e^r(\vec{q}) = \mathcal{F}_{\bar{\Delta}}\vec{\mathbf{f}}(\vec{q}) - \vec{\mathbf{f}}(\mathcal{F}_{\bar{\Delta}}\vec{q}) \quad \text{and} \quad \vec{s}_e^r(\vec{q}) = \mathcal{F}_{\bar{\Delta}}\vec{s}'(\vec{q}) - \vec{s}'(\mathcal{F}_{\bar{\Delta}}\vec{q}). \quad (3.21)$$

Both $\vec{\mathbf{f}}_e^r$ and \vec{s}_e^r need to be closed based on $\mathcal{F}_{\bar{\Delta}}\vec{q}$, so the closure modeling task is to find

$$\vec{\mathbf{f}}^r(\mathcal{F}_{\bar{\Delta}}\vec{q}) \approx \vec{\mathbf{f}}_e^r(\vec{q}) \quad \text{and} \quad \vec{s}^r(\mathcal{F}_{\bar{\Delta}}\vec{q}) \approx \vec{s}_e^r(\vec{q}) \quad (3.22)$$

approximations. Hereafter, we only consider the filtered variables and omit $\mathcal{F}_{\bar{\Delta}}$ for conciseness. A variable q denotes either $\mathcal{F}_{\bar{\Delta}}q$ if $q \in \{\rho, p\}$ or $\mathcal{F}_{\bar{\Delta}}\rho q / \mathcal{F}_{\bar{\Delta}}\rho$ if $q \in \{\mathbf{u}, T, Y\}$.

The SGS models $\vec{\mathbf{f}}^r$ and \vec{s}^r are compositions of elementary NNs $\in \mathcal{N}$ and TVD NNs, trained toward (3.22). We represent them as

$$\vec{\mathbf{f}}^r(\vec{q}; \vec{\theta}_f) = \begin{bmatrix} \mathbf{0} \\ \mathbf{f}_{\mathbf{u}} \\ \mathbf{f}_{\mathbf{u}} \cdot \mathbf{u} + \rho \mathbf{f}_T \\ \rho \mathbf{f}_Y \end{bmatrix} \quad \text{and} \quad \vec{s}^r(\vec{q}; \vec{\theta}_s) = \begin{bmatrix} 0 \\ \mathbf{0} \\ Q s_{\mathcal{N}} \\ -s_{\mathcal{N}} \end{bmatrix} \dot{\omega}(\vec{q}), \quad (3.23)$$

where

$$\mathbf{f}_{\mathbf{u}} = \begin{bmatrix} f_{\mathcal{N},11}(\vec{q}; \vec{\theta}_{f_{11}}) & f_{\mathcal{N},12}(\vec{q}; \vec{\theta}_{f_{12}}) & f_{\mathcal{N},13}(\vec{q}; \vec{\theta}_{f_{13}}) \\ f_{\mathcal{N},21} & f_{\mathcal{N},22}(\vec{q}; \vec{\theta}_{f_{22}}) & f_{\mathcal{N},23}(\vec{q}; \vec{\theta}_{f_{23}}) \\ f_{\mathcal{N},31} & f_{\mathcal{N},32} & f_{\mathcal{N},33}(\vec{q}; \vec{\theta}_{f_{33}}) \end{bmatrix} \quad (3.24)$$

closes the momentum equations. It is composed of 6 independent NNs $\in \mathcal{N}$, where the symmetry is enforced by letting $f_{\mathcal{N},ji} = f_{\mathcal{N},ij}$ for $(i, j) \in \{(1, 2), (1, 3), (2, 3)\}$. Fluxes

$$\mathbf{f}_T = \begin{bmatrix} f_{T1} \\ f_{T2} \\ f_{T3} \end{bmatrix} \quad \text{and} \quad \mathbf{f}_Y = \begin{bmatrix} f_{Y1} \\ f_{Y2} \\ f_{Y3} \end{bmatrix} \quad (3.25)$$

close the energy and species equations, where f_{Ti} and f_{Yi} are taken to be coupled. That is, each pair (f_{Ti}, f_{Yi}) is the output from a single TVD NN:

$$\vec{f}_{c1}(\vec{q}; \vec{\theta}_{c1}) = \begin{bmatrix} f_{T1} \\ f_{Y1} \end{bmatrix}, \quad \vec{f}_{c2}(\vec{q}; \vec{\theta}_{c2}) = \begin{bmatrix} f_{T2} \\ f_{Y2} \end{bmatrix}, \quad \text{and} \quad \vec{f}_{c3}(\vec{q}; \vec{\theta}_{c3}) = \begin{bmatrix} f_{T3} \\ f_{Y3} \end{bmatrix}. \quad (3.26)$$

The TVD NN in (3.9) is extended to a system of equations and is used for \vec{f}_{ci} as

$$\begin{aligned} \vec{f}_{ci}(\vec{q}; \vec{\theta}_{ci}) = & \frac{1}{2} \left[\vec{f}_{\mathcal{N},ci}(\vec{q}_c^{i+}; \vec{\theta}_{f_{ci}}) + \vec{f}_{\mathcal{N},ci}(\vec{q}_c^{i-}; \vec{\theta}_{f_{ci}}) - a(\vec{\theta}_{f_{ci}})(\vec{q}_c^{i+} - \vec{q}_c^{i-}) \right] \\ & - \left[\left| \vec{\nu}_{\mathcal{N},ci}^+(\vec{q}; \vec{\theta}_{\nu_{ci}^+}) \right| + \vec{\psi}_i(\vec{q}_c) \odot \vec{\nu}_{\mathcal{N},ci}^-(\vec{q}; \vec{\theta}_{\nu_{ci}^-}) \right] \odot \frac{\Delta_i \vec{q}_c}{\Delta x_i}, \end{aligned} \quad (3.27)$$

forming $\vec{\theta}_{ci} = [\vec{\theta}_{f_{ci}}; \vec{\theta}_{\nu_{ci}^+}; \vec{\theta}_{\nu_{ci}^-}]$, for $i \in \{1, 2, 3\}$. The symbol \odot indicates component-wise multiplication. In (3.27), $\vec{q}_c = [\hat{T}, Y]^\top$ is a vector of reactive scalars with the normalized temperature $\hat{T} = T/T_0$, $\vec{q}_c^{i\pm}$ the slope-limited reconstruction of \vec{q}_c , $\vec{\psi}_i$ the anti-diffusive flux limiter (3.11) for each component of \vec{q}_c , and $\Delta_i \vec{q}_c / \Delta x_i$ the finite-differenced gradient of \vec{q}_c , all in the x_i -direction. The T -component of the raw output of \vec{f}_{ci} , f_{Ti} , is multiplied by T_0 for normalization. More details of the NN formulation can be found in A.3.

The NN SGS stress \mathbf{f}_u for the momentum is not constrained because, without bounds corresponding to $Y \in [0, 1]$, the lack of smoothness of the velocity field is less consequential. That is, there is nothing qualitatively incorrect for any small error in \mathbf{u} . To retain consistency with the momentum equations, $\mathbf{f}_u \cdot \mathbf{u} = \{f_{\mathcal{N},ij} u_j\}_{i=1}^3$ is added to the total energy equation. Finally, the NN correction for the non-conservative source term $s_{\mathcal{N}}$ is added to the equations for the reactive scalars, which is multiplied by $\dot{\omega}(\vec{q})$ so it becomes active only near the flame where $\dot{\omega}(\vec{q}) \approx 0$. The NN $s_{\mathcal{N}}$ also does not require constraint, although its effect on the smoothness of the solution is not yet fully explored. All NN models in (3.23)— $f_{\mathcal{N},ij}$ for momentum, $\vec{f}_{\mathcal{N},ci}$ and $\vec{\nu}_{\mathcal{N},ci}^\pm$ for scalars, and $s_{\mathcal{N}}$ —share the baseline architecture:

$$f_{\mathcal{N},ij}, s_{\mathcal{N}} \in \mathcal{N}(39 \rightarrow 50 \rightarrow 1), \quad \vec{f}_{\mathcal{N},ci} \in \mathcal{N}(2 \rightarrow 50 \rightarrow 2), \quad \vec{\nu}_{\mathcal{N},ci}^\pm \in \mathcal{N}(39 \rightarrow 50 \rightarrow 2) \quad (3.28)$$

for $i \in \{1, 2, 3\}$ and $j \geq i$.

To generate a training dataset, DNS is run on a rectangular domain as in Fig. 10, discretized as a uniform structured staggered mesh with $256 \times 256 \times 4096$ points. A standard fourth-order Runge–Kutta (RK4) method is used—given a PDE $\partial_t \vec{q} = \vec{R}(\vec{q})$,

$$\begin{aligned} \vec{q}^{n,1} &= \vec{q}^{n,0} + \frac{\Delta t}{2} \vec{R}(\vec{q}^{n,0}) \\ \vec{q}^{n,2} &= \vec{q}^{n,0} + \frac{\Delta t}{2} \vec{R}(\vec{q}^{n,1}) \\ \vec{q}^{n,3} &= \vec{q}^{n,0} + \Delta t \vec{R}(\vec{q}^{n,2}) \\ \vec{q}^{n+1,0} &= \vec{q}^{n,4} = \vec{q}^{n,0} + \Delta t \sum_{s=1}^4 w_s \vec{R}(\vec{q}^{n,s-1}), \end{aligned} \quad (3.29)$$

for $\vec{q}^n = \vec{q}^{n,0}$ at time step n with the weights $w_s = [\frac{1}{6}, \frac{1}{3}, \frac{1}{3}, \frac{1}{6}]^\top$. Then, the DNS solutions are box-filtered

$$F_{\bar{\Delta}}(\mathbf{x}) = \begin{cases} 1/\bar{\Delta}^3 & \|\mathbf{x}\|_\infty \leq \bar{\Delta}/2 \\ 0 & \text{otherwise} \end{cases}, \quad (3.30)$$

with the filter size of $\bar{\Delta}/\Delta_{\text{DNS}} = 16$, which is then downsampled to the LES grid of $\Delta_{\text{LES}} = \bar{\Delta}$ with the grid size of $16 \times 16 \times 256$.

For every gradient-descent iteration, a minibatch size of $M = 20$ is randomly sampled from the total $\mathcal{M} = 1000$ DNS snapshots. LES predictions are initialized with the downsampled filtered DNS field at a time stamp $t_0^{(m)}$ of the m -th snapshot for $m \in \{1, 2, \dots, M\}$. The NN model leads to the LES solution \vec{q} by numerically integrating

$$\partial_t \vec{q} + \nabla \cdot [\vec{\mathbf{f}}(\vec{q}) + \vec{\mathbf{f}}^r(\vec{q}; \vec{\theta}_f)] = [\vec{s}(\vec{q}) + \vec{s}^r(\vec{q}; \vec{\theta}_s)] \quad (3.31)$$

on $t \in [t_0^{(m)}, t_0^{(m)} + t_f]$ with RK4 (3.29) for some simulation time t_f . Then, following previous efforts with embedded SGS NN models [2, 8], the parameters

$$\vec{\theta} = \left[\{\vec{\theta}_{f_{ij}}\}_{i=1, j \geq i}^3; \{\vec{\theta}_{f_{ei}}\}_{i=1}^3; \{\vec{\theta}_{\nu_{\pm i}}\}_{i=1}^3; \vec{\theta}_s \right] \quad (3.32)$$

are trained *a posteriori*, to minimize the averaged loss

$$\mathcal{J} = \frac{1}{M} \sum_{m=1}^M \mathcal{J}^{(m)} = \frac{1}{M} \sum_{m=1}^M \int_{\Omega} \left\| \vec{q}_p(\mathbf{x}, t_0^{(m)} + t_f; \vec{\theta}) - \vec{q}_{p,e}(\mathbf{x}, t_0^{(m)} + t_f) \right\|_W^2 d\mathbf{x}, \quad (3.33)$$

which measures the mismatch between the NN-predicted solution of primitive variables $\vec{q}_p \equiv [\rho, \mathbf{u}, \hat{T}, Y]^\top$ and the trusted data $\vec{q}_{p,e}$ —downsampled filtered DNS data—within a region of interest Ω at time $t_0^{(m)} + t_f$ for all $m \in \{1, 2, \dots, M\}$. We use a weighted norm

$$\|\vec{v}\|_W^2 = \vec{v}^\top W \vec{v} \quad \text{with} \quad W = \text{diag}(0, 1, 1, 1, 3, 3), \quad (3.34)$$

which normalizes the mismatch of each variable, where the coefficients are selected based on predictions. The mismatch of ρ is not included since the Favre-filtered continuity equation does not require closure, though including it might warrant investigation. The simulation time t_f is selected to be short enough that the sensitivity does not explode [34]. We choose $t_f = 0.1$ which corresponds to 200 LES time steps with $\Delta t_{\text{LES}} = 5 \times 10^{-4}$.

For comparison, an unconstrained NN model is tested where

$$\vec{\mathbf{f}}^r(\vec{q}; \vec{\theta}_f) = \begin{bmatrix} \mathbf{0} \\ \mathbf{f}_u \\ \mathbf{f}_u \cdot \mathbf{u} + \mathbf{f}_T \\ \mathbf{f}_Y \end{bmatrix} \quad \text{and} \quad \vec{s}^r(\vec{q}; \vec{\theta}_s) = \begin{bmatrix} 0 \\ \mathbf{0} \\ Q s_{\mathcal{N}} \\ -s_{\mathcal{N}} \end{bmatrix} \dot{\omega}(\vec{q}), \quad (3.35)$$

which matches (3.23) but all entries of $\mathbf{f}_T = \{f_{\mathcal{N}, T_i}\}_{i=1}^3$ and $\mathbf{f}_Y = \{f_{\mathcal{N}, Y_i}\}_{i=1}^3$ are unconstrained NN models $\in \mathcal{N}(39 \rightarrow 50 \rightarrow 1)$. Again, raw outputs of $f_{\mathcal{N}, T_i}$ are multiplied by T_0 for normalization.

A penalized model using (3.35) is also tested for comparison, where the bounded $Y \in [0, 1]$ property is sought by penalizing the loss as

$$\mathcal{J} = \frac{1}{M} \sum_{m=1}^M \left[\mathcal{J}^{(m)} + \int_{\Omega} P(Y(\mathbf{x}, t_0^{(m)} + t_f; \vec{\theta})) d\mathbf{x} \right] \quad (3.36)$$

with

$$P(Y) = \begin{cases} Y^2 & Y < 0 \\ (Y - 1)^2 & Y > 1 \\ 0 & \text{otherwise,} \end{cases} \quad (3.37)$$

which penalizes out-of-bound values.

All NN parameters are Xavier initialized, while the weights of the output layer W^5 are initialized as zero to prevent overshoots. Adam [35] is used as the optimizer, with the base learning rate of 10^{-3} and L_2 regularization with the regularization constant of $\lambda = 10^{-2}$. Additional details of the numerical simulations, the NN formulation, and the optimization are in A.

The TVD NN method far outperforms the others. Figure 8 shows \hat{T} and Y predicted by the unconstrained, penalized, and TVD NN models on a two-dimensional slice of the computational domain. The prediction is out of sample in the sense that it is made at $t = 1$, 2000 time steps from the initial flow field (about one large-eddy turnover time), which is well beyond the 200 time steps ($t_f = 0.1$) used for training. In this case, the unconstrained and penalized NNs both lead to unphysical fluctuations in both \hat{T} and Y fields, which are most obvious away from the flame where both should be uniform. Although there is no strict constraint on \hat{T} that it can fluctuate at large wavelengths as pressure waves are resolved, small-scale oscillations near \hat{T}_{\min} for the unconstrained and penalized models are unphysical. The TVD NN successfully suppresses the oscillations in both scalar fields, except one $Y < 0$ region, for which potential reasons will be discussed in Section 4.1. Still, the violation is milder than that for the other models, as in Fig. 9.

4 Additional Discussion

This section further discusses the approach and its results, particularly for the turbulent combustion problem, including additional factors to consider and potential opportunities.

4.1 Comments on the turbulent flame results from Section 3.5

It was seen in Fig. 8 that the non-oscillatory (boundedness) property is significantly improved, but we emphasize it may not be exactly preserved. There are several potential reasons for this, which warrant discussion.

First, the NN terms are coupled with the existing physical source terms. Physical solutions can oscillate, as can discretizations of them, irrespective of the added NN closure. If the numerical scheme used for the represented terms allows oscillations, then the solution is not guaranteed to be non-oscillatory since it is not fully represented with the constrained NN. There is only an expectation that the added NN closure itself will not contribute to them. Specifically, while conservative flux divergence terms in (3.15) can be constrained by upwinding the flux as in A.2, there is no simple way to exactly constrain non-conservative source terms to preclude oscillations. Of course, there exist standard approaches for this issue [36], but their generalization

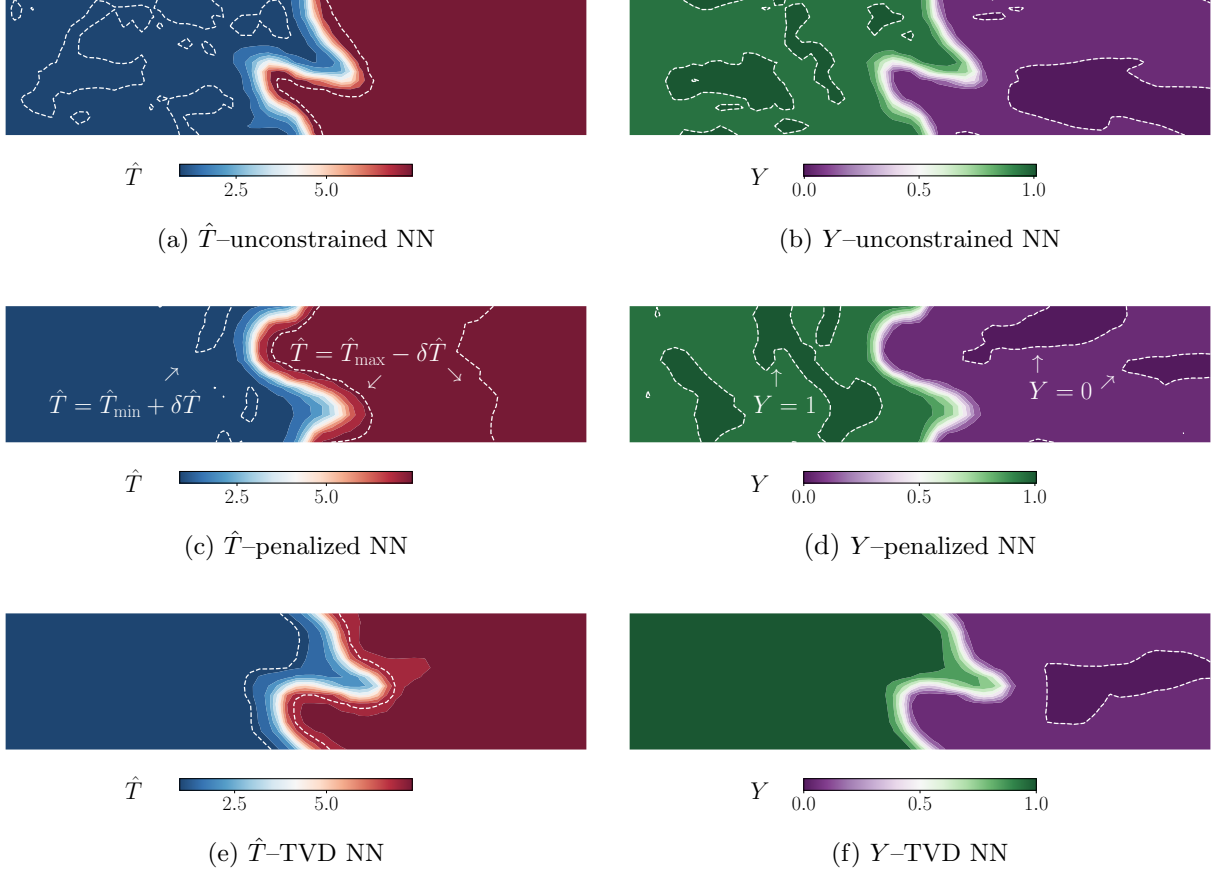


Figure 8: Turbulent flame LES: (a) normalized temperature $\hat{T} = T/T_0$ and (b) reactant mass fraction Y for the unconstrained model (3.35); (c) \hat{T} and (d) Y for the model (3.35) with penalization (3.36); and (e) \hat{T} and (f) Y for the TVD NN model (3.23). Dashed contours in (a), (c), and (e) indicate where $\hat{T} = \hat{T}_{\max} - \delta\hat{T}$ or $\hat{T} = \hat{T}_{\min} + \delta\hat{T}$ with $\delta\hat{T} = 10^{-2}(\hat{T}_{\max} - \hat{T}_{\min})$; those in (b), (d), and (f) indicate where $Y = 0$ or $Y = 1$: enclosed regions are out of bound $Y \notin [0, 1]$. The bound $Y \leq 1$ is exactly satisfied in (f).

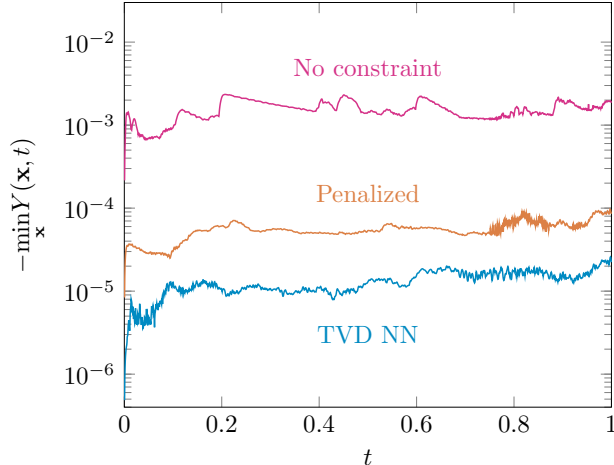


Figure 9: Violations of the $Y \geq 0$ constraint: magnitude of minimum Y values for all cases.

to our reacting Navier–Stokes equations is cumbersome. Moreover, the effect of the source term closure $s_{\mathcal{N}}$ may exacerbate the inexactness of the physical source term, which has not yet been considered and is left for future work.

Second, the performance of the multi-dimensional extension of the scheme has not been considered in detail. Although the common practice for the extension is to apply a one-dimensional scheme in each dimension, the full consequences are unexplored, and there are possibly additional performance opportunities.

Lastly, the effect of using the standard RK4 (3.29) is unknown since the TVD property of our model has only been verified for the forward Euler scheme. A safer choice is a TVD time-stepper that preserves TVD property, such as the Strong Stability Preserving Runge–Kutta (SSP RK) methods [37]. However, it should be noted that the TVD time steppers preserve such property only when used in conjunction with an exact TVD numerical flux. Since only the NN closure terms are made TVD, not the whole discretization to avoid dissipation that degrades turbulence, there is no significant advantage anticipated for a TVD time scheme. We used (3.29) as it is accurate and convenient, unlike SSP RK methods that require auxiliary operators for more than third-order accurate schemes [37]. Moreover, the adjoint of (3.29) needed to compute sensitivities $d\mathcal{J}/d\vec{\theta}$ for (3.33) has been derived previously [38]. Despite such benefits and the success seen in Fig. 8, its potential inexactness still needs further investigation.

4.2 Alternate base schemes

We adapted the KT scheme to NN for its efficiency. Most non-oscillatory finite-volume schemes are upwind, which requires characteristic decomposition for application to systems of equations. This generally requires iterative methods, which make the differentiation (by hand or with AD) needed more complex. Central schemes avoid this, and the KT scheme is one of the most concise among them. That said, there is no impediment for other established schemes including upwind schemes to be adapted to the new NN closure.

As a central scheme, the model can be further modified, especially in the reconstruction step. The slope-limited reconstruction (2.13) is not necessary for the non-oscillatory property but for minimizing the numerical dissipation and improving accuracy. For that, one could employ different slope limiters, as the KT scheme [25] is compatible with other options including the monotonized central limiter $\phi(r) = \max[0, \min(2r, 0.5(r+1), 2)]$. Additional reconstruction methods can also be adapted, such as Weighted ENO (WENO) reconstruction [39]. Although WENO reconstruction is typically used for upwind schemes, it can also be applied to central schemes [29], so it should be compatible with the specific formulation introduced. Note that for higher-order reconstruction for systems, additional benefits should come from computing the exact spectral radius of the NN flux Jacobian (2.20) instead of estimating it from the (2.22) 1-norm, although the needed eigenvalue decomposition would make differentiation more challenging.

Finally, one can replace the differentiation (2.15) with a less expensive approximation. As $f'_{\mathcal{N}}$ is a function of $\vec{\theta}$ and affects the loss, the NN training requires the gradient of $f'_{\mathcal{N}}$ with respect to $\vec{\theta}$. The gradient $d\mathcal{J}/d\vec{\theta}$ includes the $\partial_{f'_{\mathcal{N}}}\mathcal{J}\partial_{\vec{\theta}}f'_{\mathcal{N}}$ component from the chain rule, where $\partial_{\vec{\theta}}f'_{\mathcal{N}}$ is then a second-order derivative of $f_{\mathcal{N}}$, $\partial_{\vec{\theta}}f'_{\mathcal{N}} = \partial_{\vec{\theta}}\partial_{q^{\pm}}f_{\mathcal{N}}(q^{\pm})$, which increases the cost of NN training. Finite difference is an alternative,

$$f'_{\mathcal{N}}(q_{i+\frac{1}{2}}^{\pm}) \approx \frac{f_{\mathcal{N}}(q_{i+1}) - f_{\mathcal{N}}(q_i)}{q_{i+1} - q_i}, \quad (4.1)$$

but this is challenging when $q_{i+1} \approx q_i$, so we chose (2.15), which is more expensive but exact.

4.3 General applicability

We have formulated the model, particularly (3.9), so it can learn both hyperbolic and parabolic PDEs. Extending the discussion from the first paragraph of Section 3.4, this was important for a NN closure to be capable of learning the needed physics. We anticipate that the modified model covers a wide class of conservation laws with suitable closures for unknown or unrepresented physics. For learning higher-order dynamics, either providing a wider stencil to the NNs or adding more complexities to the NN itself should suffice. Including fully nonlocal effects, such as forms of radiation, would necessitate significant redesign. We can anticipate that the proposed model may be challenged if asked to learn PDEs with non-conservative source terms since the formulation is in a conservative form. In this scenario, an additional NN source term should probably be introduced, as in (3.23), though the investigation of its effect on the non-oscillatory property is left for future work.

A final remark is that the TVD NN is not guaranteed to stay exactly constrained when applied to out-of-sample data. Recall that $\vec{\theta}$ is constrained within the feasible set in (2.25), and the maximum wave speed is evaluated only over the training samples. That is,

$$\mathcal{C} = \left\{ \vec{\theta} \mid \max_{q \in \mathcal{Q}_{\text{train}}} a(\vec{\theta}) \Big|_q \leq \text{CFL}_{\text{max}} \Delta x / \Delta t \right\}, \quad (4.2)$$

where $\mathcal{Q}_{\text{train}}$ is the training dataset of q . Hence, if the trained model is evaluated on $q \notin \mathcal{Q}_{\text{train}}$, there is no strict guarantee that the predicted solution is non-oscillatory. The hope is that q is similar enough to

some $q' \in \mathcal{Q}_{\text{train}}$ that the model preserves this property well enough. In other words, inclusive $\mathcal{Q}_{\text{train}}$ will provide robustness. This suggests that training a model *a posteriori* is likely more robust than training it *a priori*, since $\mathcal{Q}_{\text{train}} = \{q(\mathbf{x}, t) \mid t \in [t_0^{(m)}, t_0^{(m)} + t_f]\}_{m=1}^M$ for the *a posteriori* training in (3.33), for example, is more abundant than $\mathcal{Q}_{\text{train}} = \{q(\mathbf{x}, t_0^{(m)})\}_{m=1}^M$ for the corresponding *a priori* training, though the proposed scheme is not limited to either of the approaches.

Acknowledgments

This material is based in part upon work supported by the Department of Energy, National Nuclear Security Administration, under Award Number DE-NA0003963.

A Additional Details for Turbulent Flame Simulations

A.1 Nondimensionalization

We derive (3.15) from its dimensional form:

$$\frac{\partial}{\partial t^\star} \begin{bmatrix} \rho^\star \\ \rho^\star \mathbf{u}^\star \\ E^\star \\ \rho^\star Y \end{bmatrix} + \nabla^\star \cdot \begin{bmatrix} \rho^\star \mathbf{u}^\star \\ \rho^\star \mathbf{u}^\star \mathbf{u}^\star + p^\star \mathbf{I} - \boldsymbol{\tau}^\star \\ \mathbf{u}^\star (E^\star + p^\star) - \boldsymbol{\tau}^\star \cdot \mathbf{u}^\star + \boldsymbol{\varphi}_T^\star \\ \rho^\star \mathbf{u}^\star Y + \boldsymbol{\varphi}_Y^\star \end{bmatrix} = \begin{bmatrix} 0 \\ \mathbf{0} \\ Q^\star \dot{\omega}^\star \\ -\dot{\omega}^\star \end{bmatrix}, \quad (\text{A.1})$$

where \star denotes a dimensional quantity. By definition, the reactant mass fraction Y is already dimensionless. Constitutive relations for diffusive fluxes are

$$\boldsymbol{\tau}^\star = \mu^\star \left[\nabla^\star \mathbf{u}^\star + (\nabla^\star \mathbf{u}^\star)^\top - \frac{2}{3} (\nabla^\star \cdot \mathbf{u}^\star) \mathbf{I} \right], \quad \boldsymbol{\varphi}_T^\star = -k^\star \nabla^\star T^\star, \quad \boldsymbol{\varphi}_Y^\star = -\rho^\star \mathcal{D}^\star \nabla^\star Y, \quad (\text{A.2})$$

where diffusivities are T^\star dependent as

$$\frac{\mu^\star}{\mu_0^\star} = \frac{k^\star / c_p^\star}{k_0^\star / c_{p,0}^\star} = \frac{\rho^\star \mathcal{D}^\star}{\rho_0^\star \mathcal{D}_0^\star} = \left(\frac{T^\star}{T_0^\star} \right)^{0.7}. \quad (\text{A.3})$$

The subscript 0 denotes the unburnt state, and we assume a constant specific heat capacity at constant pressure, so $c_p^\star = c_{p,0}^\star$. The ideal gas equation of state is

$$p^\star = \rho^\star \mathcal{R}_{\text{sp}}^\star T^\star, \quad (\text{A.4})$$

with the specific gas constant $\mathcal{R}_{\text{sp}}^\star$, and the Arrhenius law

$$\dot{\omega}^\star = A^\star \rho^{\star 2} Y \exp(-T_a^\star / T^\star), \quad (\text{A.5})$$

with the Arrhenius constant A^\star and the activation temperature T_a^\star .

Reynolds number	Re	2500
Prandtl number	Pr	0.1
Schmidt number	Sc	0.1
Unburnt gas temperature	T_0	2353
Arrhenius constant	A	2500
Heat release ratio	α	0.863
Zel'dovich number	β	5.49
Heat capacity ratio	γ	1.17

Table 1: Dimensionless parameters.

We use the length scale ℓ_F^* and the velocity scale u_F^* from the forcing scheme discussed in A.2.1, the unburnt gas density ρ_0^* , and the specific heat capacity c_p^* to nondimensionalize. The resulting nondimensional variables are

$$\mathbf{x} = \frac{\mathbf{x}^*}{\ell_F^*}, \quad \mathbf{u} = \frac{\mathbf{u}^*}{u_F^*}, \quad t = \frac{t^* u_F^*}{\ell_F^*}, \quad \rho = \frac{\rho^*}{\rho_0^*}, \quad p = \frac{p^*}{\rho_0^* u_F^{*2}}, \quad \text{and} \quad T = \frac{c_p^* T^*}{u_F^{*2}}, \quad (\text{A.6})$$

and we define $T_0 = c_p^* T_0^* / u_F^{*2}$ the nondimensional reference temperature. Diffusive fluxes (A.2) become (3.18), as we define

$$\text{Re} = \frac{\rho_0^* u_F^* \ell_F^*}{\mu_0^*}, \quad \text{Pr} = \frac{\mu_0^* c_p^*}{k_0^*}, \quad \text{and} \quad \text{Sc} = \frac{\mu_0^*}{\rho_0^* \mathcal{D}_0^*}, \quad (\text{A.7})$$

with $\mu = \mu^* / \mu_0^* = (T/T_0)^{0.7}$. The equation of state becomes $p = (\gamma - 1)\rho T / \gamma$, and the Arrhenius law becomes

$$\dot{\omega} = \underbrace{A^* \rho_0^{*2} \exp(-T_a^*/T_f^*)}_{\equiv A} \rho^2 Y \exp\left(\frac{T_a^*}{T_f^*} - \frac{T_a^*}{T^*}\right) = A \rho^2 Y \exp\left[\frac{\beta}{\alpha} \left(1 - \frac{T_f}{T}\right)\right], \quad (\text{A.8})$$

with $\alpha = (T_f^* - T_0^*)/T_f^*$ and $\beta = \alpha T_a^*/T_f^*$, where T_f^* is the dimensional adiabatic flame temperature.

Parameter values in Table 1 are adapted from Towery *et al.* [33]. The reference temperature T_0 is elevated to lower the Mach number $\text{Ma} = 1/\sqrt{(\gamma - 1)T_0}$ to prevent unwanted transition to detonation following Poludnenko & Oran [40].

A.2 Numerical procedures

Figure 10 provides a schematic of the simulation configuration. Both DNS and LES are in a rectangular spatial domain:

$$\mathbf{x} = [x_1, x_2, x_3]^\top \in [-L/2, L/2] \times [-L/2, L/2] \times [-8L, 8L] \quad (\text{A.9})$$

with $L = 1$, uniformly discretized as $\Delta x_1 = \Delta x_2 = \Delta x_3$. The flame will be statistically planar on the $x_1 x_2$ -plane and the normal to the x_3 -direction. The grid is staggered where \mathbf{u} and $\rho \mathbf{u}$ are stored at cell faces normal to the coordinate axes, and the other state variables are stored at cell centers [41, 42, 43]. Second-order finite differences are used to compute the spatial derivatives, and second-order linear interpolation is

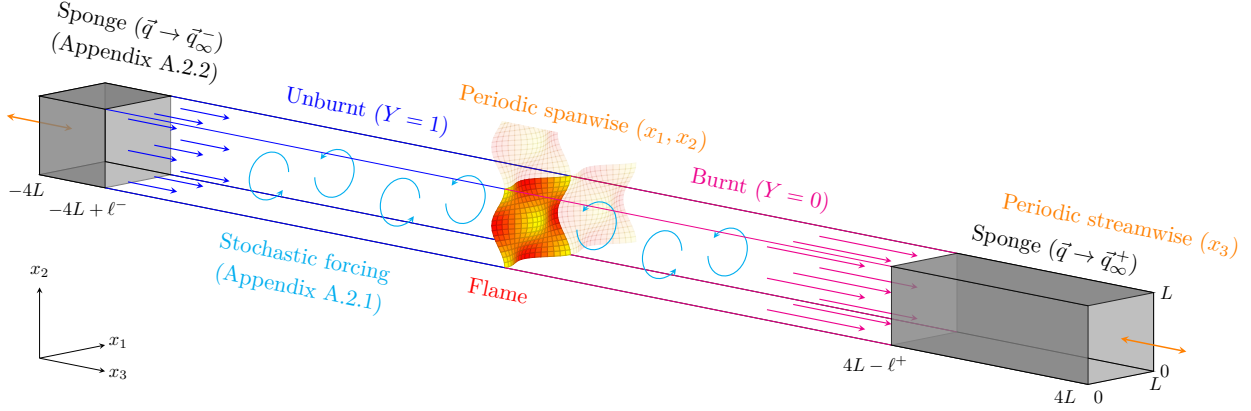


Figure 10: Schematic of the turbulent flame simulation.

used to interpolate from a cell center to cell faces or vice versa. In the total energy equation and the species equation, scalar advection is upwind to suppress spurious oscillations, where scalar values (T and Y) are reconstructed on the cell face. Following Larroturou [44], this is done by piecewise linear reconstruction with Superbee [45] limiting. Momenta $\rho \mathbf{u}$ need not be reconstructed as they already exist on cell faces.

The turbulent flame simulation is developed in stages: (1) a non-reacting forced isotropic turbulence is generated [46] (A.2.1); (2) once the isotropic turbulence is statistically stationary, a laminar flame is superimposed onto the turbulent flow field by re-initializing the ρ , T , and Y fields; and (3) the turbulent flame is allowed to become statistically stationary before data are used. The flame propagates in the $+x_3$ -direction so $Y = 1$ near the $-x_3$ -boundary and $Y = 0$ near the $+x_3$ -boundary. The spatial domain is set as periodic in all dimensions, and the discontinuity at the x_3 -boundary is relieved in a sponge layer [47] on each end (details of this are in A.2.2). The turbulence forcing and the sponge are implemented as source terms in the governing equations:

$$\partial_t \vec{q} + \nabla \cdot \vec{\mathbf{f}}(\vec{q}) = \vec{s}(\vec{q}) + \vec{s}_{\text{forcing}} + \vec{s}_{\text{sponge}}. \quad (\text{A.10})$$

A.2.1 Turbulence forcing

The turbulence forcing scheme was developed by Eswaran and Pope [46] and is formulated as

$$\vec{s}_{\text{forcing}} = \begin{bmatrix} 0 \\ \rho \mathbf{b} \\ \rho \mathbf{u} \cdot \mathbf{b} - \rho \mathbb{E}[\dot{\epsilon}] \\ 0 \end{bmatrix}, \quad (\text{A.11})$$

where \mathbf{b} is sampled from an Ornstein–Uhlenbeck (OU) process every time step, and $\mathbb{E}[\dot{\epsilon}]$ is the expected energy injection rate by the forcing. Subtracting constant $\mathbb{E}[\dot{\epsilon}]$ from the total energy keeps the internal energy stationary, so the forcing only excites the kinetic energy. It has been shown [46] that $\mathbb{E}[\dot{\epsilon}] =$

$4N_{\boldsymbol{\kappa}}\sigma_F^2\tau_F$, where $N_{\boldsymbol{\kappa}}$ is the total number of discrete wavenumber vectors $\boldsymbol{\kappa}$ being forced, σ_F^2 the variance of the OU process, and τ_F its correlation time. Once the turbulence is statistically stationary, it can be assumed that the kinetic energy dissipation rate converges to $\mathbb{E}[\dot{e}]$, meaning that a desired value of dissipation rate can be achieved by setting the energy injection rate. As τ_F is the most energetic time scale of isotropic turbulence, it is also an approximate integral time scale, so an approximate integral length scale can be defined as $\ell_F = (\mathbb{E}[\dot{e}]\tau_F^3)^{1/2}$. Since length scales and velocity scales are nondimensionalized by ℓ_F and $u_F \equiv \ell_F/\tau_F$ respectively, $\mathbb{E}[\dot{e}] = 1$. Forcing is applied to $N_{\boldsymbol{\kappa}} = 26$ modes: $\boldsymbol{\kappa}/\kappa_0 \in \{(\pm 1, 0, 0), (0, \pm 1, 0), (0, 0, \pm 1), (\pm 1, \pm 1, 0), (\pm 1, 0, \pm 1), (0, \pm 1, \pm 1), (\pm 1, \pm 1, \pm 1)\}$, where $\kappa_0 = 2\pi/L$, so $\sigma_F^2 = 1/104$.

A.2.2 Absorbing sponge zone boundary regions

The sponge zone drives the state toward a target condition with the damping term $\vec{s}_{\text{sponge}} = -\zeta(\mathbf{x})(\vec{q} - \vec{q}_{\infty})$, where the damping strength is

$$\zeta(\mathbf{x}) = \begin{cases} 200[(x_3^- - x_3)/\ell^-]^3 & x_3 \leq x_3^- \\ 0 & x_3^- < x_3 < x_3^+ \\ 200[(x_3 - x_3^+)/\ell^+]^3 & x_3^+ \leq x_3 \end{cases}. \quad (\text{A.12})$$

In (A.12), x_3^{\pm} is the x_3 -coordinate where the sponge layer starts, and ℓ^{\pm} is the thickness of the sponge layer. Since sound propagates faster in the burnt region than in the unburnt region, the sponge layer is set to be thicker in the burnt region: $\ell^+ = 3L$ and $\ell^- = L$, which yields $x_3^+ = 5L$ and $x_3^- = -7L$.

The target conditions are

$$\vec{q}_{\infty} = \begin{cases} \vec{q}_{\infty}^- & x_3 \leq x_3^- \\ \vec{q}_{\infty}^+ & x_3 \geq x_3^+ \end{cases} \quad (\text{A.13})$$

where

$$\vec{q}_{\infty}^+ = \begin{bmatrix} \rho_b \\ 0 \\ 0 \\ \rho_b[\alpha s_L/(1-\alpha) + s_T] \\ T_0/\gamma + \rho_b[\alpha s_L/(1-\alpha) + s_T]^2/2 \\ 0 \end{bmatrix} \quad \text{and} \quad \vec{q}_{\infty}^- = \begin{bmatrix} \rho_0 \\ 0 \\ 0 \\ \rho_0 s_T \\ T_0/\gamma + \rho_0 s_T^2/2 \\ \rho_0 \end{bmatrix}, \quad (\text{A.14})$$

with ρ_0 and $\rho_b = (1-\alpha)\rho_0$ the densities of the unburnt and burnt gas respectively, s_L the laminar flame speed which can be estimated [1]:

$$s_L = \sqrt{\frac{2A(1-\alpha)^{2-n}}{\text{Re Pr}\beta^2}}, \quad (\text{A.15})$$

and s_T is the average turbulent flame speed (related to the time-averaged global fuel consumption rate)

$$s_T = \frac{1}{\rho_0 L^2 \tau_{\text{avg}}} \int_{t_0}^{t_0 + \tau_{\text{avg}}} \int_{\Omega} \dot{\omega}(\mathbf{x}, t) d\mathbf{x} dt. \quad (\text{A.16})$$

Time-averaging is over time $\tau_{\text{avg}} = 10$, and Ω is the physical region of the domain, which is the entire domain aside from the buffer zones. Iterations showed that $s_T \approx 2.5$, so setting $s_T = 2.5$ approximately anchors the flame in the middle of the domain.

A.3 NN formulation

For any unconstrained NN in (3.23) and (3.35), both the input and the output are stored at cell centers. At a grid point \mathbf{x} , its input is composed of discrete values of primitive variables $\vec{q}_p = [\rho, \mathbf{u}, \hat{T}, Y]^\top$ at \mathbf{x} and the neighboring points:

$$\vec{\mathcal{I}}[\vec{q}_p](\mathbf{x}) = \begin{bmatrix} \{\rho(\mathbf{x}); \hat{T}(\mathbf{x}); Y(\mathbf{x})\} \in \mathbb{R}^3 \\ \{\rho(\mathbf{x} \pm \mathbf{\Delta}_i) - \rho(\mathbf{x})\}_{i=1}^3 \in \mathbb{R}^6 \\ \{\mathbf{u}(\mathbf{x} \pm \mathbf{\Delta}_i) - \mathbf{u}(\mathbf{x})\}_{i=1}^3 \in \mathbb{R}^{18} \\ \{\hat{T}(\mathbf{x} \pm \mathbf{\Delta}_i) - \hat{T}(\mathbf{x})\}_{i=1}^3 \in \mathbb{R}^6 \\ \{Y(\mathbf{x} \pm \mathbf{\Delta}_i) - Y(\mathbf{x})\}_{i=1}^3 \in \mathbb{R}^6 \end{bmatrix} \in \mathbb{R}^{39}, \quad (\text{A.17})$$

where $\mathbf{\Delta}_i = \Delta x_i \mathbf{e}_i$ with \mathbf{e}_i the unit vector in x_i . The input consists of 3 scalar variables $[\rho, \hat{T}, Y]^\top$ at \mathbf{x} and both forward (between $\mathbf{x} + \mathbf{\Delta}_i$ and \mathbf{x}) and backward (between $\mathbf{x} - \mathbf{\Delta}_i$ and \mathbf{x}) differences of 6 primitive variables \vec{q}_p in 3 spatial dimensions $[x_1, x_2, x_3]^\top$, yielding 39 total input variables per mesh point. Pointwise values of \mathbf{u} are excluded for Galilean invariance. Therefore, $f_{\mathcal{N},ij}$, $s_{\mathcal{N}}$, and $\{f_{\mathcal{N},Ti}\}_{i=1}^3$ and $\{f_{\mathcal{N},Yi}\}_{i=1}^3$ for unconstrained models are all $\in \mathcal{N}(39 \rightarrow 50 \rightarrow 1)$. As outputs are originally at cell centers, those of $f_{\mathcal{N},ij}$ are linearly interpolated to cell faces.

Constrained models, $\vec{f}_{\mathcal{N},ci}$ and $\vec{v}_{\mathcal{N},ci}^\pm$, are evaluated at cell faces. The NN $\vec{f}_{\mathcal{N},ci}$ takes only the reactive scalars $\vec{q}_c = [\hat{T}, Y]^\top$ as the input as

$$\vec{f}_{\mathcal{N},ci}(\vec{q}_c^\pm(\mathbf{x} + \mathbf{\Delta}_i/2)) \in \mathcal{N}(2 \rightarrow 50 \rightarrow 2), \quad (\text{A.18})$$

where

$$\begin{aligned} \vec{q}_c^+(\mathbf{x} + \mathbf{\Delta}_i/2) &= \vec{q}_c(\mathbf{x} + \mathbf{\Delta}_i) - 0.5\phi[\vec{r}_i(\mathbf{x} + \mathbf{\Delta}_i)][\vec{q}_c(\mathbf{x} + 2\mathbf{\Delta}_i) - \vec{q}_c(\mathbf{x} + \mathbf{\Delta}_i)] \quad \text{and} \\ \vec{q}_c^-(\mathbf{x} + \mathbf{\Delta}_i/2) &= \vec{q}_c(\mathbf{x}) + 0.5\phi[\vec{r}_i(\mathbf{x})][\vec{q}_c(\mathbf{x} + \mathbf{\Delta}_i) - \vec{q}_c(\mathbf{x})] \end{aligned} \quad (\text{A.19})$$

are the slope-limited reconstructions with the slope ratio

$$\vec{r}_i(\mathbf{x}) = \frac{\vec{q}_c(\mathbf{x}) - \vec{q}_c(\mathbf{x} - \mathbf{\Delta}_i)}{\vec{q}_c(\mathbf{x} + \mathbf{\Delta}_i) - \vec{q}_c(\mathbf{x})}. \quad (\text{A.20})$$

For the NN diffusivity, $\vec{v}_{\mathcal{N},ci}^\pm$ takes the 39 inputs

$$\vec{v}_{\mathcal{N},ci}^\pm(\mathbf{x} + \mathbf{\Delta}_i/2) = \vec{v}_{\mathcal{N},ci}^\pm[\vec{\mathcal{I}}[\vec{q}_p](\mathbf{x} + \mathbf{\Delta}_i/2)] \in \mathcal{N}(39 \rightarrow 50 \rightarrow 2), \quad (\text{A.21})$$

where $\vec{\mathcal{I}}[\vec{q}_p](\mathbf{x} + \mathbf{\Delta}_i/2) = [\vec{\mathcal{I}}[\vec{q}_p](\mathbf{x}) + \vec{\mathcal{I}}[\vec{q}_p](\mathbf{x} + \mathbf{\Delta}_i)]/2$.

A.4 Adjoint-based stochastic gradient descent

In the one-dimensional demonstrations, the end-to-end sensitivity $d\mathcal{J}/d\vec{\theta}$ was computed using the full AD supported by PyTorch [22]. However, computing sensitivities solely based on AD can be slow and require excessive memory for a complex system, particularly for *a posteriori* NN training for three-dimensional simulations. An efficient alternative is to directly formulate and solve adjoint governing equations [2, 8]. This is identical to the full AD method in that they both solve the dual of the primal problem (A.10). However, direct solving of adjoint equations is less expensive than the full AD since it leverages the prior knowledge on all the operations, whereas the full AD method tracks all the operations *ad hoc* with unnecessary intermediate values or gradient-tracking features, adding cost.

For a PDE solution $\vec{q}(\mathbf{x}, t; \vec{\theta})$ on $t \in [t_0^{(m)}, t_0^{(m)} + t_f]$ starting from a time stamp $t_0^{(m)}$ as in (3.33), sensitivities are computed using adjoints as

$$\frac{d\mathcal{J}^{(m)}}{d\vec{\theta}} = \int_{\Omega} \left(\sum_{n=0}^{N_t-1} \sum_{s=1}^4 w_s \vec{q}^{\dagger n, s} \cdot \frac{\partial \vec{R}}{\partial \vec{\theta}} \Big|^{n, s-1} \right) d\mathbf{x}, \quad (\text{A.22})$$

where \vec{R} is the RHS of (A.10) including the NN terms. The adjoint \vec{q}^{\dagger} of \vec{q} is obtained by solving the adjoint governing equations backward in time,

$$\begin{aligned} \vec{q}^{\dagger n, 3} &= \vec{q}^{\dagger n, 4} + \frac{\Delta t}{2} \vec{q}^{\dagger n, 4} \cdot \frac{\partial \vec{R}}{\partial \vec{q}} \Big|^{n, 3} \\ \vec{q}^{\dagger n, 2} &= \vec{q}^{\dagger n, 4} + \frac{\Delta t}{2} \vec{q}^{\dagger n, 3} \cdot \frac{\partial \vec{R}}{\partial \vec{q}} \Big|^{n, 2} \\ \vec{q}^{\dagger n, 1} &= \vec{q}^{\dagger n, 4} + \Delta t \vec{q}^{\dagger n, 2} \cdot \frac{\partial \vec{R}}{\partial \vec{q}} \Big|^{n, 1} \\ \vec{q}^{\dagger n-1, 4} &= \vec{q}^{\dagger n, 0} = \vec{q}^{\dagger n, 4} + \Delta t \sum_{s=1}^4 w_s \vec{q}^{\dagger n, s} \cdot \frac{\partial \vec{R}}{\partial \vec{q}} \Big|^{n, s-1}, \end{aligned} \quad (\text{A.23})$$

starting from the final condition

$$\vec{q}^{\dagger N_t-1, 4} = \vec{q}^{\dagger N_t, 0} = \frac{\partial D^{(m)}(\mathbf{x})}{\partial \vec{q}^{N_t, 0}} \quad (\text{A.24})$$

at time step N_t , which corresponds to $t = t_0^{(m)} + t_f$, until $n = 0$ at $t = t_0^{(m)}$. The pointwise mismatch $D^{(m)}(\mathbf{x}) = \|\vec{q}_p(\mathbf{x}, t_0^{(m)} + t_f; \vec{\theta}) - \vec{q}_{p,e}(\mathbf{x}, t_0^{(m)} + t_f)\|_2^2$ contributes to the loss as

$$\mathcal{J}^{(m)} = \int_{\Omega} D^{(m)}(\mathbf{x}) d\mathbf{x}. \quad (\text{A.25})$$

The Jacobian $\partial \vec{R} / \partial \vec{q}$ and the $\vec{q}^{\dagger N_t, 0} = \partial D^{(m)} / \partial \vec{q}$ are evaluated based on the fully discretized form of (A.10), which makes the computed sensitivity exact for the discrete system [38].

References

- [1] F. A. Williams, *Combustion Theory*. CRC Press, 2018.

- [2] J. Sirignano, J. F. MacArt, and J. B. Freund, “DPM: A deep learning PDE augmentation method with application to large-eddy simulation,” *J. Comput. Phys.*, vol. 423, p. 109811, 2020.
- [3] K. Um, R. Brand, Y. R. Fei, P. Holl, and N. Thuerey, “Solver-in-the-Loop: Learning from Differentiable Physics to Interact with Iterative PDE-Solvers,” *Adv. Neural Inf. Process. Syst.*, vol. 33, pp. 6111–6122, 2020.
- [4] J. Ling, A. Kurzawski, and J. Templeton, “Reynolds averaged turbulence modelling using deep neural networks with embedded invariance,” *J. Fluid Mech.*, vol. 807, pp. 155–166, 2016.
- [5] J.-L. Wu, H. Xiao, and E. Paterson, “Physics-informed machine learning approach for augmenting turbulence models: A comprehensive framework,” *Phys. Rev. Fluids*, vol. 3, no. 7, p. 074602, 2018.
- [6] J. Park and H. Choi, “Toward neural-network-based large eddy simulation: Application to turbulent channel flow,” *J. Fluid Mech.*, vol. 914, p. A16, 2021.
- [7] J. Ling, R. Jones, and J. Templeton, “Machine learning strategies for systems with invariance properties,” *J. Comput. Phys.*, vol. 318, pp. 22–35, 2016.
- [8] J. F. MacArt, J. Sirignano, and J. B. Freund, “Embedded training of neural-network subgrid-scale turbulence models,” *Phys. Rev. Fluids*, vol. 6, no. 5, p. 050502, 2021.
- [9] M. Raissi, P. Perdikaris, and G. E. Karniadakis, “Physics-informed neural networks: A deep learning framework for solving forward and inverse problems involving nonlinear partial differential equations,” *J. Comput. Phys.*, vol. 378, pp. 686–707, 2019.
- [10] L. Lu, P. Jin, G. Pang, Z. Zhang, and G. E. Karniadakis, “Learning nonlinear operators via DeepONet based on the universal approximation theorem of operators,” *Nat. Mach. Intell.*, vol. 3, no. 3, pp. 218–229, 2021.
- [11] J. Sirignano and K. Spiliopoulos, “DGM: A deep learning algorithm for solving partial differential equations,” *J. Comput. Phys.*, vol. 375, pp. 1339–1364, 2018.
- [12] J. H. Ferziger, M. Perić, and R. L. Street, *Computational methods for fluid dynamics*. Springer, 2019.
- [13] E. S. Levitin and B. T. Polyak, “Constrained minimization methods,” *USSR Comput. Math. Math. Phys.*, vol. 6, no. 5, pp. 1–50, 1966.
- [14] D. P. Bertsekas, “Nonlinear programming,” *J. Oper. Res. Soc.*, vol. 48, no. 3, pp. 334–334, 1997.
- [15] K. Miettinen, *Nonlinear multiobjective optimization*, vol. 12. Springer Science & Business Media, 1999.
- [16] A. S. Nair, J. Sirignano, M. Panesi, and J. F. MacArt, “Deep Learning Closure of the Navier–Stokes Equations for Transition-Continuum Flows,” *AIAA J.*, vol. 61, no. 12, pp. 5484–5497, 2023.

- [17] G. Cybenko, “Approximation by superpositions of a sigmoidal function,” *Math. Control. Signals Syst.*, vol. 2, no. 4, pp. 303–314, 1989.
- [18] Z. Chen, A. Gelb, and Y. Lee, “Learning the Dynamics for Unknown Hyperbolic Conservation Laws Using Deep Neural Networks,” *SIAM J. Sci. Comput.*, vol. 46, no. 2, pp. A825–A850, 2024.
- [19] Z. Chen, V. Churchill, K. Wu, and D. Xiu, “Deep neural network modeling of unknown partial differential equations in nodal space,” *J. Comput. Phys.*, vol. 449, p. 110782, 2022.
- [20] T. Kim and M. Kang, “Approximating Numerical Flux by Fourier Neural Operators for the Hyperbolic Conservation Laws,” *arXiv preprint arXiv:2401.01783*, 2024.
- [21] Z. Li, N. Kovachki, K. Azizzadenesheli, B. Liu, K. Bhattacharya, A. Stuart, and A. Anandkumar, “Fourier neural operator for parametric partial differential equations,” *arXiv preprint arXiv:2010.08895*, 2020.
- [22] A. Paszke, S. Gross, F. Massa, A. Lerer, J. Bradbury, G. Chanan, T. Killeen, Z. Lin, N. Gimelshein, L. Antiga, *et al.*, “Pytorch: An imperative style, high-performance deep learning library,” *Adv. Neural Inf. Process. Syst.*, vol. 32, 2019.
- [23] T. Tieleman, “Lecture 6.5-rmsprop: Divide the gradient by a running average of its recent magnitude,” *COURSERA: Neural Netw. Mach. Learn.*, vol. 4, no. 2, p. 26, 2012.
- [24] R. J. LeVeque, *Numerical methods for conservation laws*, vol. 214. Springer, 1992.
- [25] A. Kurganov and E. Tadmor, “New high-resolution central schemes for nonlinear conservation laws and convection-diffusion equations,” *J. Comput. Phys.*, vol. 160, no. 1, pp. 241–282, 2000.
- [26] P. K. Sweby, “High resolution schemes using flux limiters for hyperbolic conservation laws,” *SIAM J. Numer. Anal.*, vol. 21, no. 5, pp. 995–1011, 1984.
- [27] A. Harten, “High resolution schemes for hyperbolic conservation laws,” *J. Comput. Phys.*, vol. 135, no. 2, pp. 260–278, 1997.
- [28] H. Nessyahu and E. Tadmor, “Non-oscillatory central differencing for hyperbolic conservation laws,” *J. Comput. Phys.*, vol. 87, no. 2, pp. 408–463, 1990.
- [29] D. Levy, G. Puppo, and G. Russo, “Central WENO schemes for hyperbolic systems of conservation laws,” *ESAIM: Math. Model. Numer. Anal.*, vol. 33, no. 3, pp. 547–571, 1999.
- [30] G. A. Sod, “A survey of several finite difference methods for systems of nonlinear hyperbolic conservation laws,” *J. Comput. Phys.*, vol. 27, no. 1, pp. 1–31, 1978.
- [31] D. Veynante, A. Trouvé, K. Bray, and T. Mantel, “Gradient and counter-gradient scalar transport in turbulent premixed flames,” *J. Fluid Mech.*, vol. 332, pp. 263–293, 1997.

- [32] J. F. MacArt, T. Grenga, and M. E. Mueller, “Effects of combustion heat release on velocity and scalar statistics in turbulent premixed jet flames at low and high Karlovitz numbers,” *Combust. Flame*, vol. 191, pp. 468–485, 2018.
- [33] C. Towery, A. Poludnenko, J. Urzay, J. O’Brien, M. Ihme, and P. Hamlington, “Spectral kinetic energy transfer in turbulent premixed reacting flows,” *Phys. Rev. E*, vol. 93, no. 5, p. 053115, 2016.
- [34] S. W. Chung and J. B. Freund, “An optimization method for chaotic turbulent flow,” *J. Comput. Phys.*, vol. 457, p. 111077, 2022.
- [35] D. P. Kingma and J. Ba, “Adam: A method for stochastic optimization,” *arXiv preprint arXiv:1412.6980*, 2014.
- [36] A. Bermudez and M. E. Vazquez, “Upwind methods for hyperbolic conservation laws with source terms,” *Comput. Fluids*, vol. 23, no. 8, pp. 1049–1071, 1994.
- [37] S. Gottlieb and C.-W. Shu, “Total variation diminishing Runge–Kutta schemes,” *Math. Comput.*, vol. 67, no. 221, pp. 73–85, 1998.
- [38] R. Vishnampet, D. J. Bodony, and J. B. Freund, “A practical discrete-adjoint method for high-fidelity compressible turbulence simulations,” *J. Comput. Phys.*, vol. 285, pp. 173–192, 2015.
- [39] G.-S. Jiang and C.-W. Shu, “Efficient implementation of weighted ENO schemes,” *J. Comput. Phys.*, vol. 126, no. 1, pp. 202–228, 1996.
- [40] A. Y. Poludnenko, T. A. Gardiner, and E. S. Oran, “Spontaneous transition of turbulent flames to detonations in unconfined media,” *Phys. Rev. Lett.*, vol. 107, no. 5, p. 054501, 2011.
- [41] F. H. Harlow and J. E. Welch, “Numerical calculation of time-dependent viscous incompressible flow of fluid with free surface,” *Phys. Fluids*, vol. 8, no. 12, pp. 2182–2189, 1965.
- [42] S. Nagarajan, S. K. Lele, and J. H. Ferziger, “A robust high-order compact method for large eddy simulation,” *J. Comput. Phys.*, vol. 191, no. 2, pp. 392–419, 2003.
- [43] B. J. Boersma, “A staggered compact finite difference formulation for the compressible Navier–Stokes equations,” *J. Comput. Phys.*, vol. 208, no. 2, pp. 675–690, 2005.
- [44] B. Larrouturou, “How to preserve the mass fractions positivity when computing compressible multi-component flows,” *J. Comput. Phys.*, vol. 95, no. 1, pp. 59–84, 1991.
- [45] P. L. Roe, “Some contributions to the modelling of discontinuous flows,” *Large-scale Comput. Fluid Mech.*, pp. 163–193, 1985.
- [46] V. Eswaran and S. B. Pope, “An examination of forcing in direct numerical simulations of turbulence,” *Comput. Fluids*, vol. 16, no. 3, pp. 257–278, 1988.

- [47] J. B. Freund, “Proposed inflow/outflow boundary condition for direct computation of aerodynamic sound,” *AIAA J.*, vol. 35, no. 4, pp. 740–742, 1997.